Satellite remote sensing as a tool for monitoring earthquake- and volcano-related ground deformation

Bryan J. Marfito, Janine L. Israel, Winchelle Ian G. Sevilla, Mabelline T. Cahulogan, Arturo S. Daag and Renato U. Solidum Jr.

Remote Sensing Research & Development for Natural Hazards & Disasters

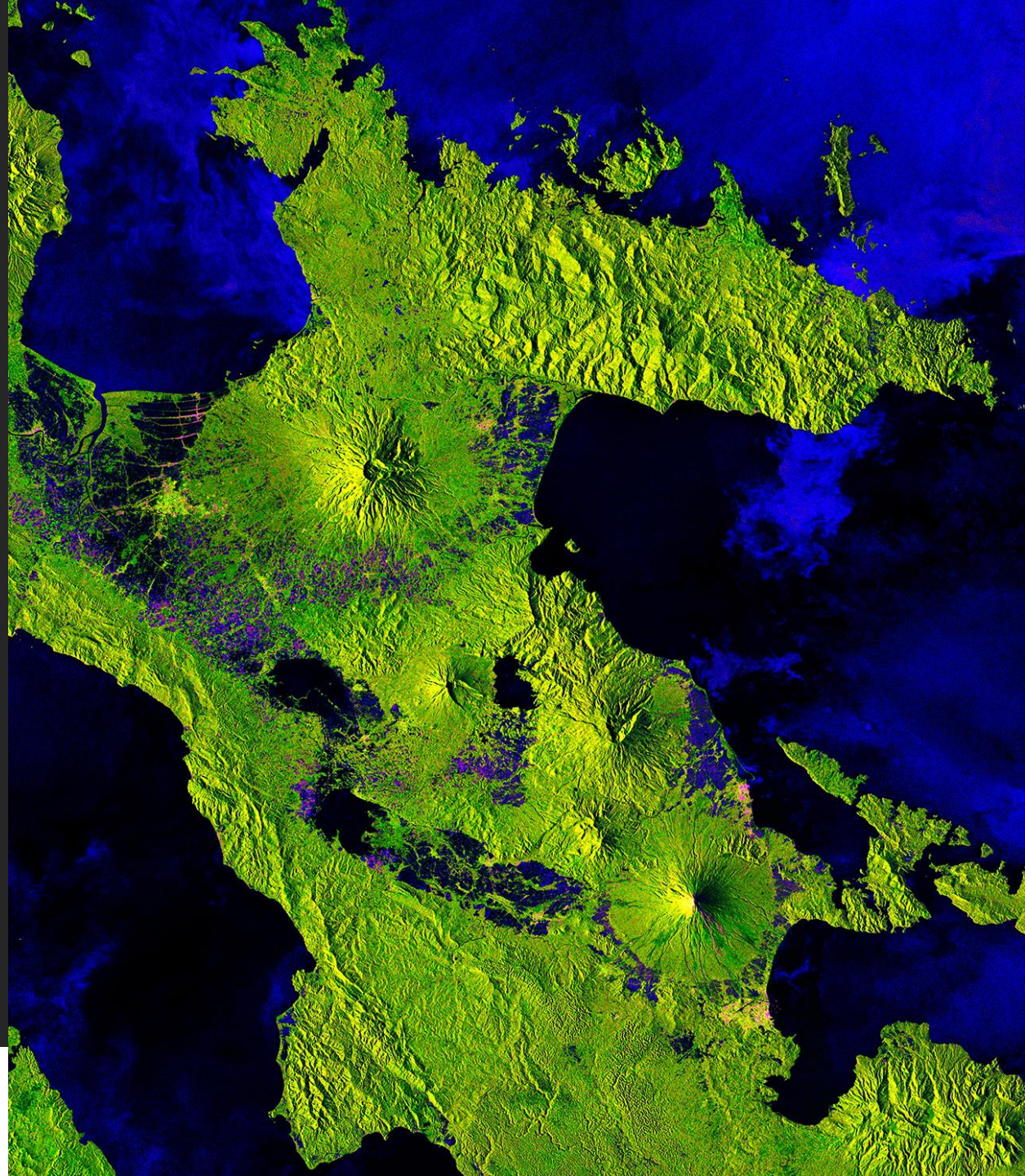

Sentinel Asia

OUTLINE

I. INTRODUCTION

II. INSTRUMENTS AND PROCESSING

III. USES OF DINSAR

IV. OUTPUTS

V. CONCLUSION

VI. WAY FORWARD

I. INTRODUCTION

What is remote sensing?

- Remote Sensing - art and science of observing an object without having a physical contact with it (Lillesand et al., 2015)
- Two types of remote sensing based on energy source
  - Active remote sensing
  - Passive remote sensing
- Three types of remote sensing based on sensor
  - Optical – visible light
  - Infrared – thermal infrared, short and medium wavelength infrared
  - Radar – microwave, radio

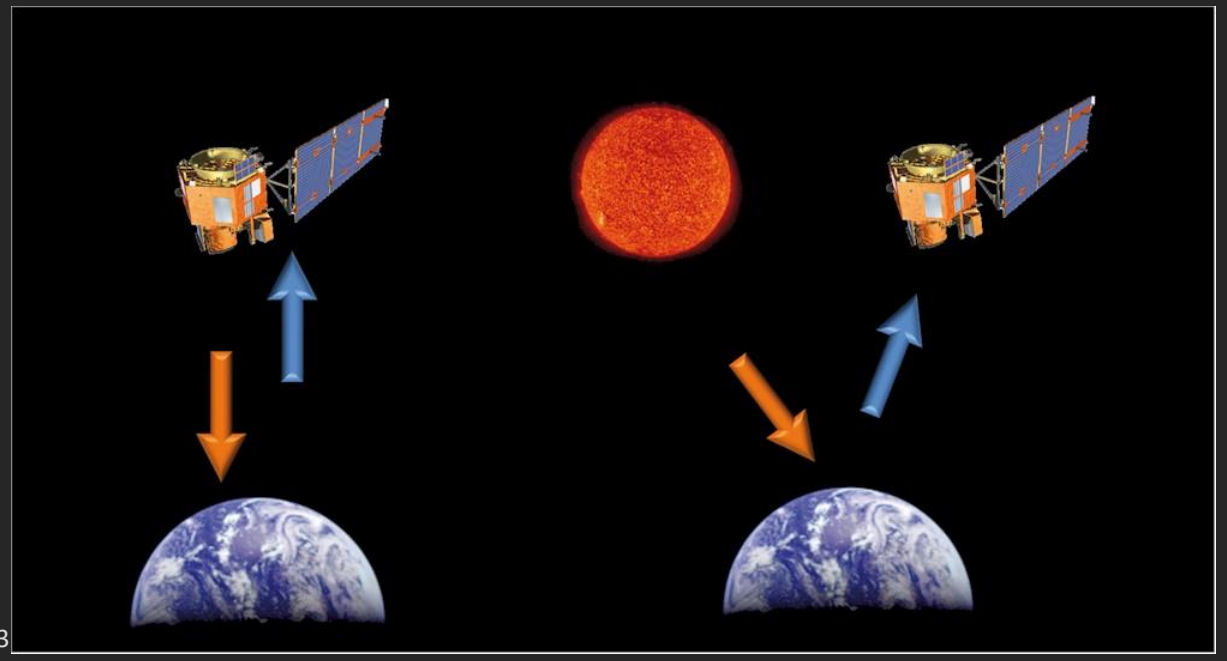

Hennig, 2013

Active Passive

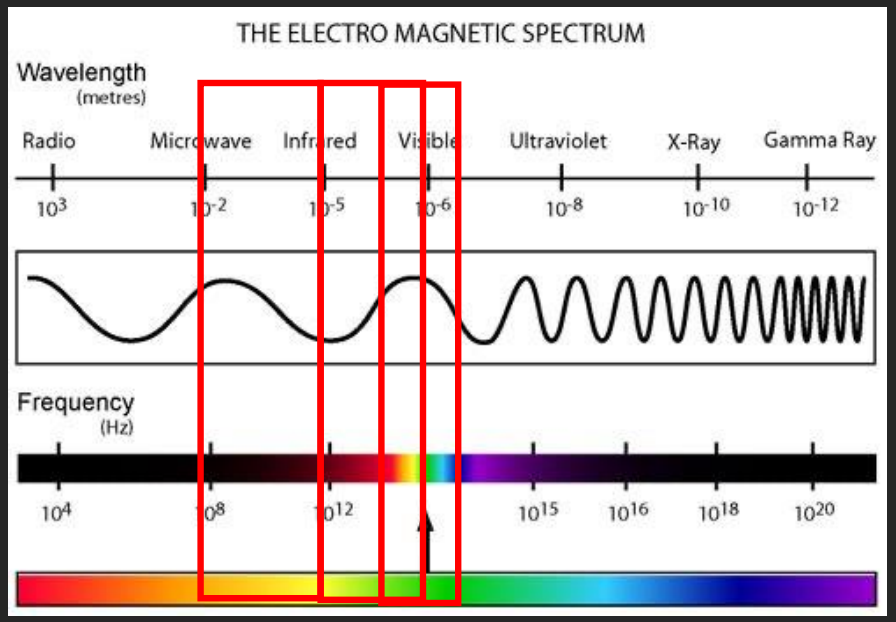

OpenStax, 2019

What is InSAR?

- Interferometric Synthetic Aperture Radar
  - Phase data from interference or superimposition of EM waves from different viewing angle (parallax) generates topography of an area
  - Uses repeated pulses to replicate a large antenna
  - Microwave EM spectrum

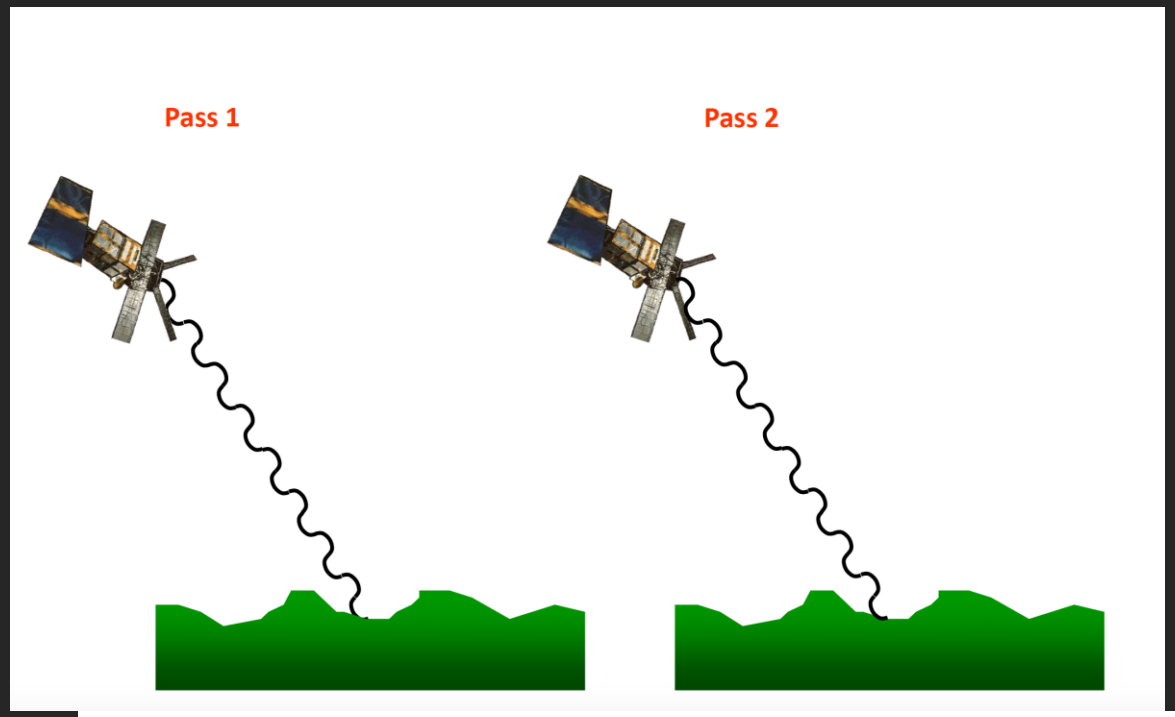

What is DInSAR?

- Differential + InSAR
- Generated by the pre- and post-event images from a satellite
- If a DEM is used to remove topography, InSAR could be used to measure displacement

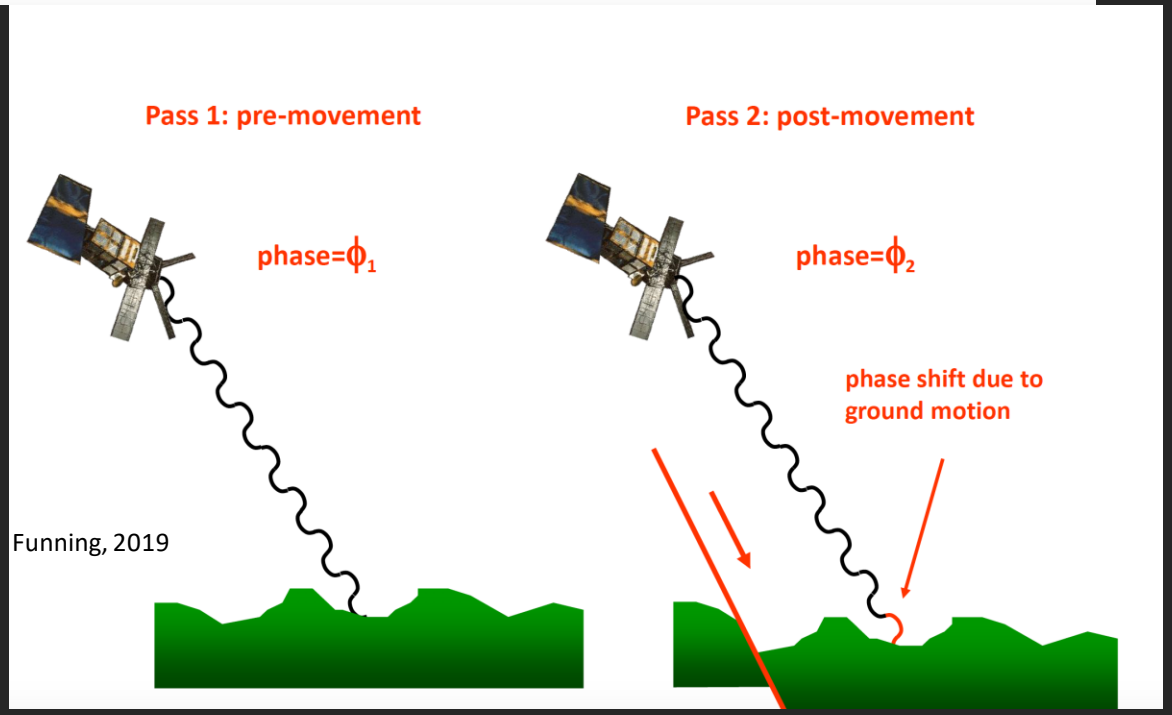

Geometry of Radar Image

- Radar image of Pinatubo Volcano (7 April 2014)
- Different geometrical characteristics as opposed to optical remote sensing due to sidescan method of acquisition

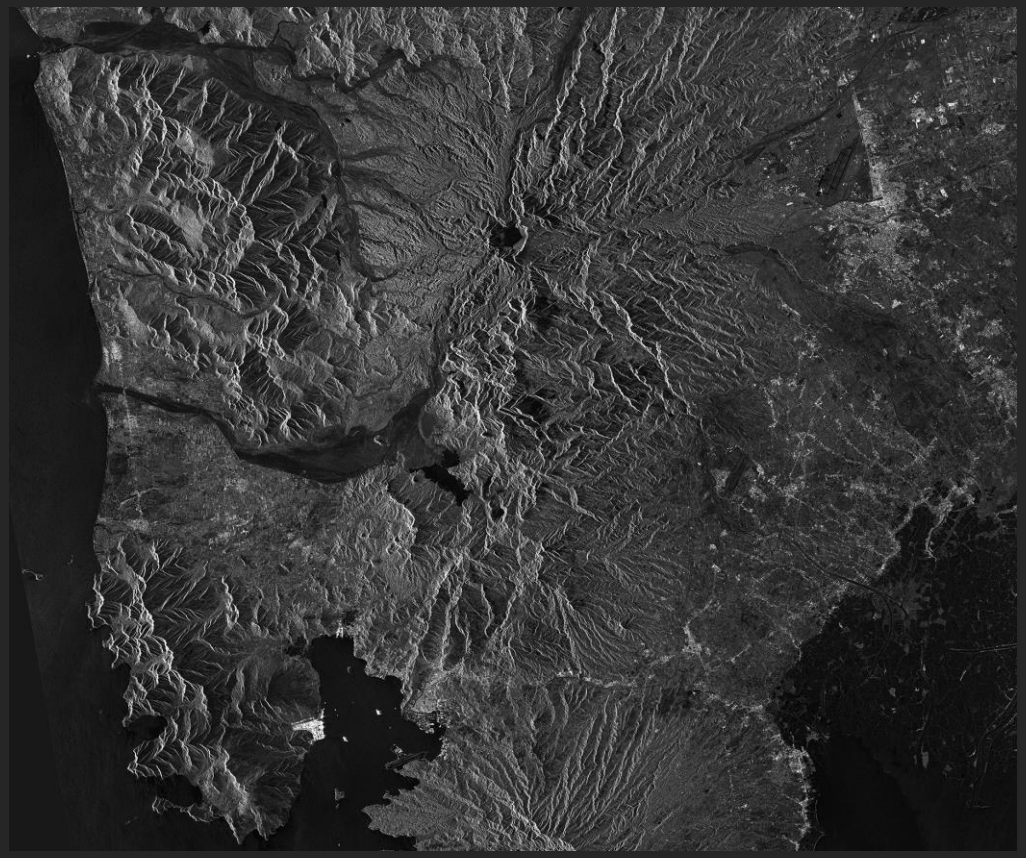

ESA, 2014

Radar Image Coordinate System

II. INSTRUMENTS AND PROCESSING

TABLE 1. COMMONLY USED FREQUENCY BANDS FOR SAR SYSTEMS AND THE CORRESPONDING FREQUENCY AND WAVELENGTH RANGES. APPLICATION EXAMPLES ARE: 1) FOLIAGE PENETRATION, SUBSURFACE IMAGING AND BIOMASS ESTIMATION IN P- AND L-BAND; 2) AGRICULTURE, OCEAN, ICE OR SUBSIDENCE MONITORING IN L-, C-, S- AND X-BAND; 3) SNOW MONITORING IN X- AND KU-BAND; AND 4) VERY HIGH-RESOLUTION IMAGING IN X- AND KA-BAND. MOST USED FREQUENCY BANDS ARE L-, C- AND X-BAND.

Frequency Band	Ka	Ku	X	C	S	L	P
Frequency [GHz]	40–25	17.6–12	12–7.5	7.5–3.75	3.75–2	2–1	0.5–0.25
Wavelength [cm]	0.75–1.2	1.7–2.5	2.5–4	4–8	8–15	15–30	60–120

Moreira et al., 2013

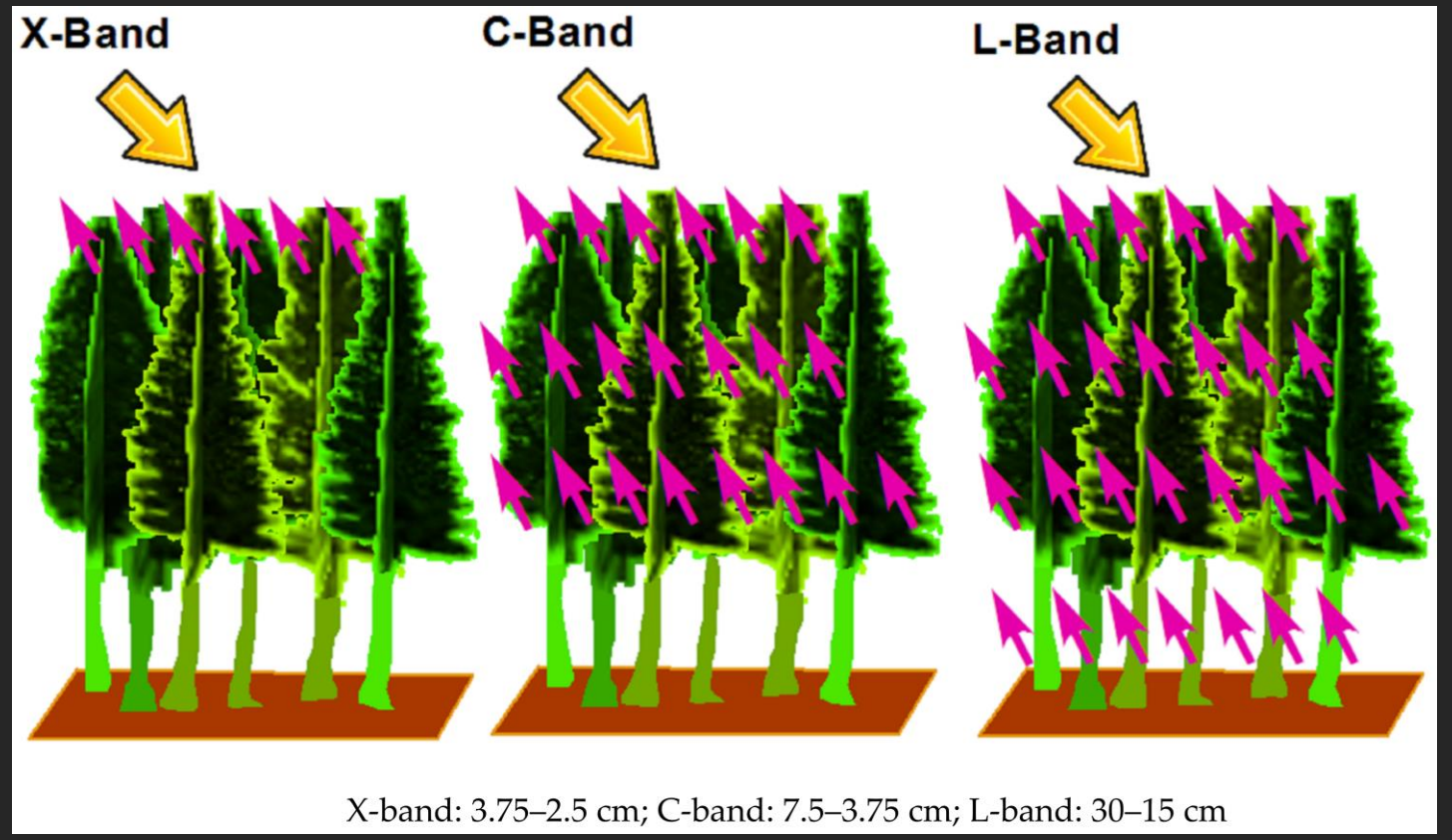

X-band: 3.75–2.5 cm; C-band: 7.5–3.75 cm; L-band: 30–15 cm

Pham et al., 2019

Sentinel 1-A & B

- Pair of earth observation satellites launched by ESA
- Orbit
  - Sun synchronous orbit with declination of 98.16°
  - 6 day (pair of satellites) or 12 day (single satellite) repeat pass on same area
- Center frequency = 5.405 GHz (C-band)
- Incidence angle = 20° to 46°
- Look direction = right
- 1 fringe = approx. 3 cm of LOS displacement

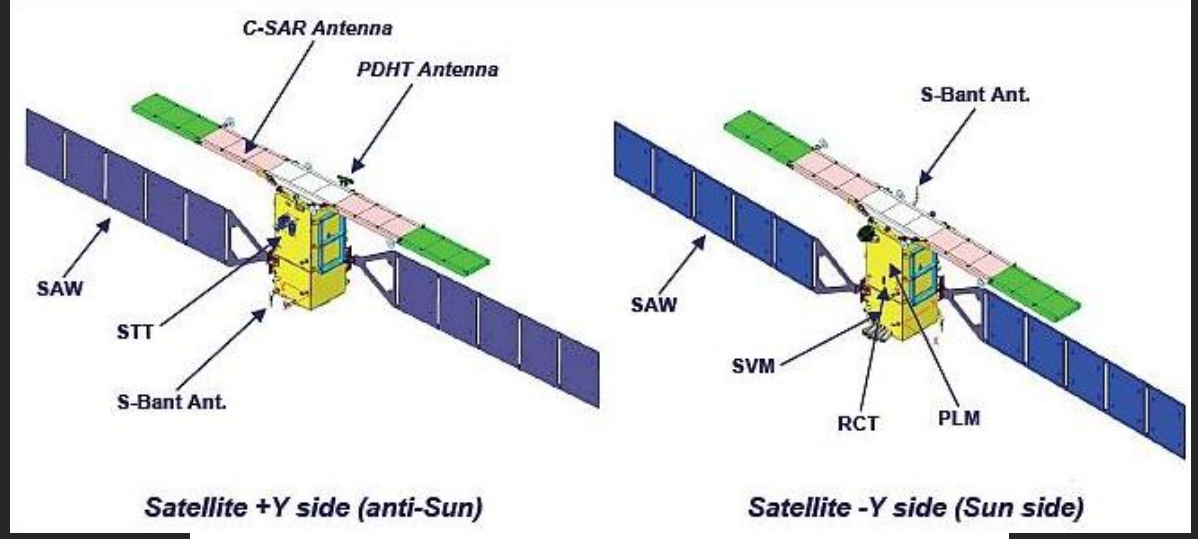

ESA, 2019a

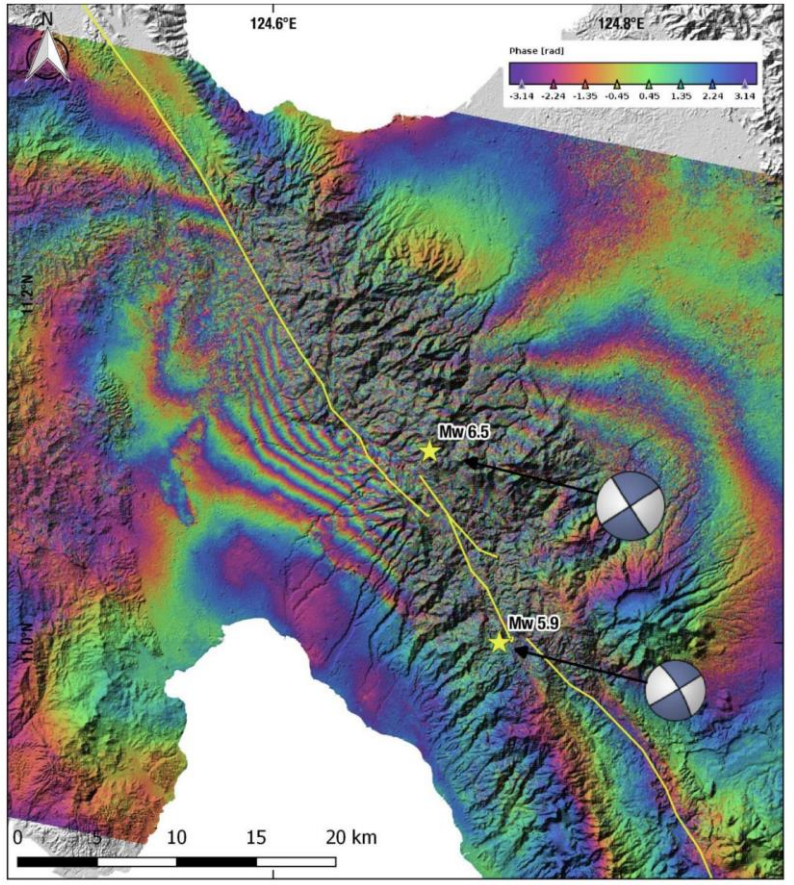

Valkaniotis et al., 2017

ALOS-2

- Satellite launched by JAXA last 4 May 2014
- Orbit:
  - Sun synchronous orbit with declination of 97.9^{o}
  - 14 day repeat pass on same area
- Center frequency = 1.25 GHz (L-band)
- Incidence angle = 8^{o} to 70^{o}
- Look direction = right or left
- 1 fringe = approx. 12 cm of displacement

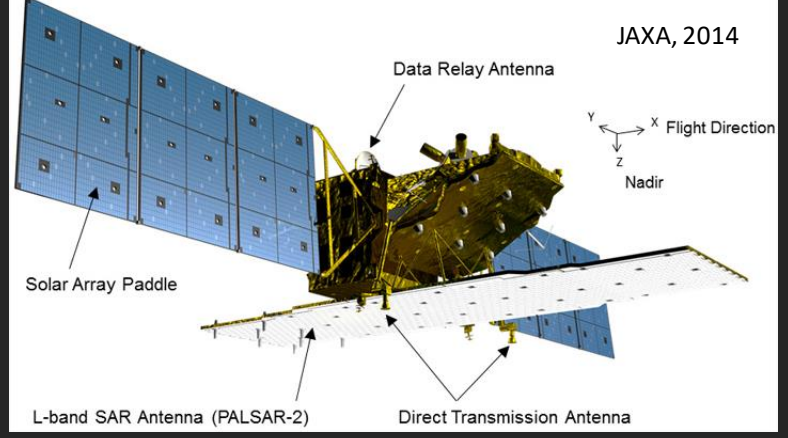

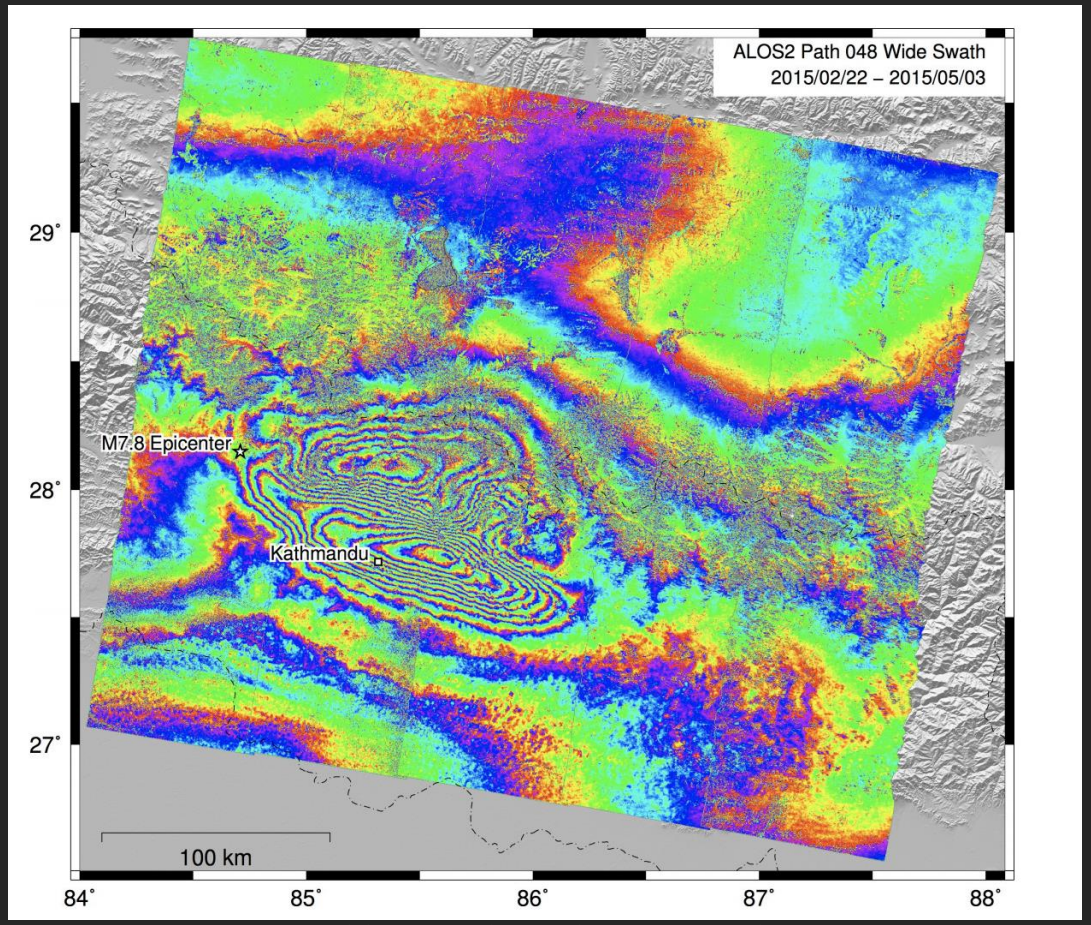

2015 M_W7.8 Gorkha Earthquake in Nepal

Lindsey et al., 2015

DInSAR processing

- Coregistration of InSAR and DEM basemap
  - Alignment of pre- and post- event InSAR images
  - Transforming the coordinates of DEM data from geocoordinates to radar coordinates
  - For time series analysis:
    - Resampling of slave images with respect to the master image
    - Stacking of slave images
- Generation of interferogram
  - Two complex images are combined to produced an interferogram
- Filtering
  - Increasing the signal to noise ratio (SNR)
  - Remove topography and ionospheric noise
- Unwrapping
- Geocoding and modeling
  - Transforming the coordinates of interferogram and LOS into geocoordinates
  - For time-series analysis, generation of velocity map using SBAS (Berardino et al., 2002)
  - Comparison with other geodetic methods

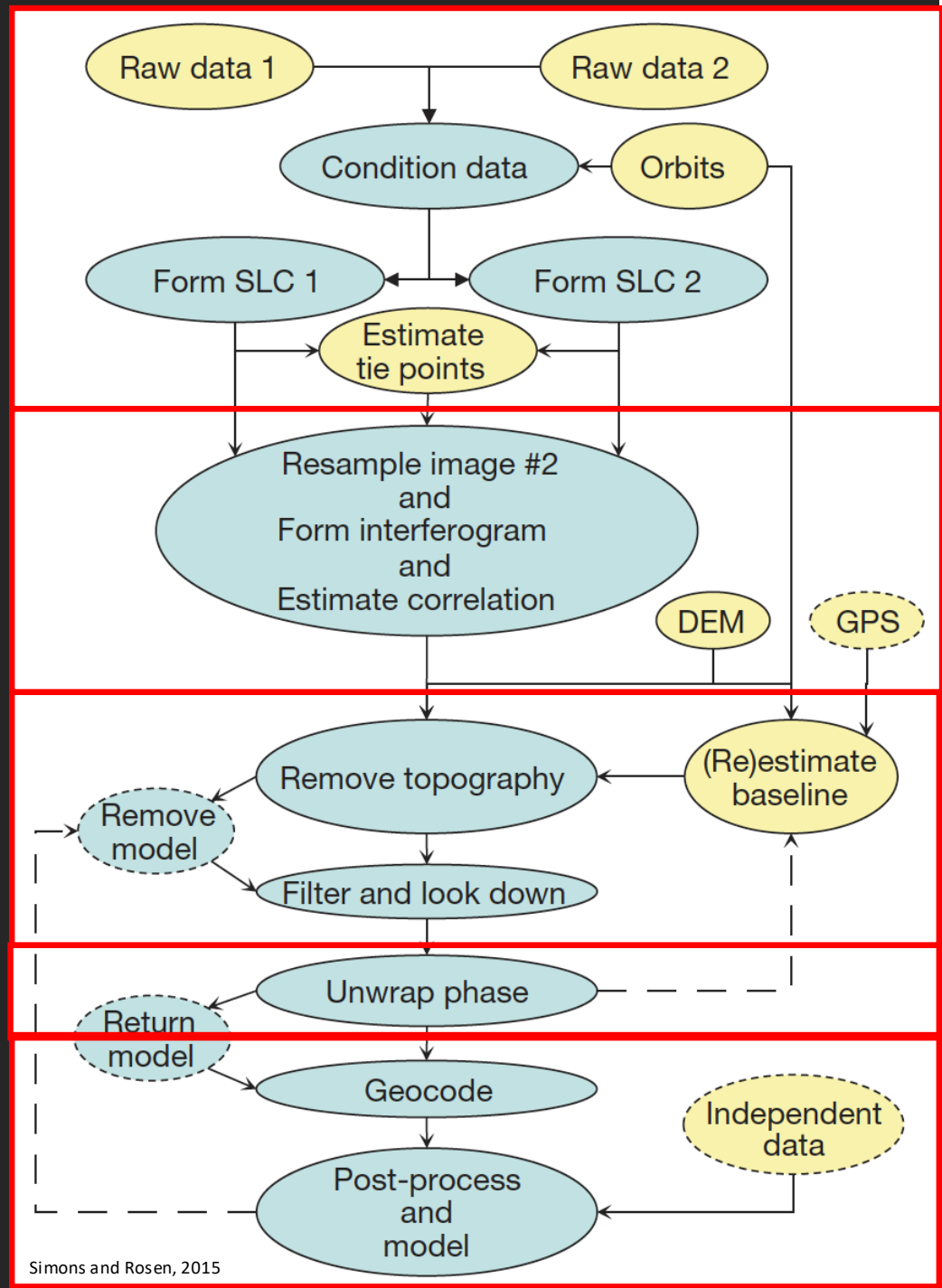

DInSAR processing softwares

- SNAP
  - GUI processing software developed by ESA to process Sentinel data
  - It could also process ALOS-2 images
  - Ease of use due to presence of graph builder and batch processing modules

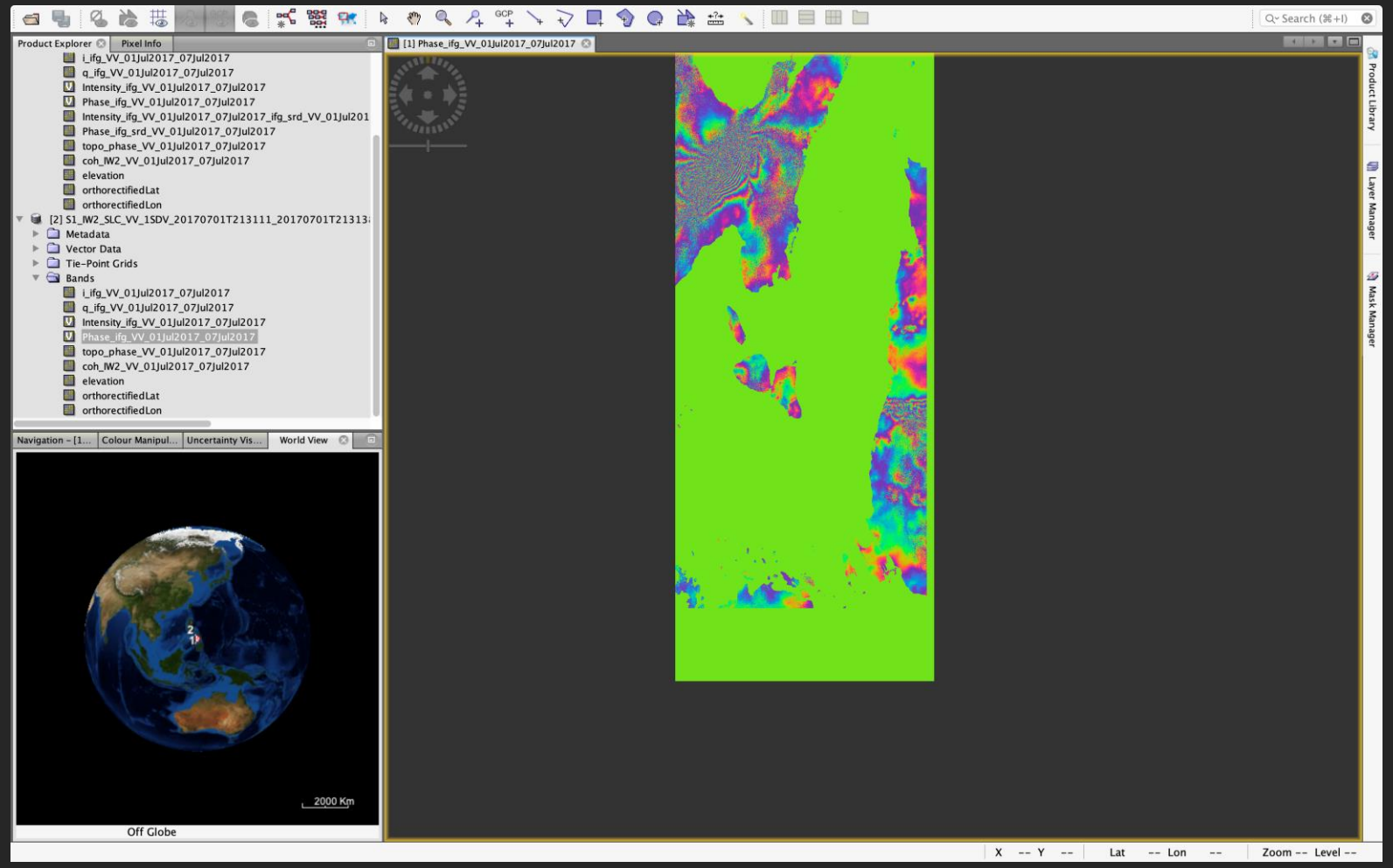

DInSAR processing softwares

- GMTSAR
  - Developed by the Scripps Institute of Oceanography
  - Doesn’t have GUI
  - Uses bash scripts to process InSAR images
  - This software could process many types of InSAR satellite data such as Sentinel 1, ALOS-2, Radarsat, Envisat

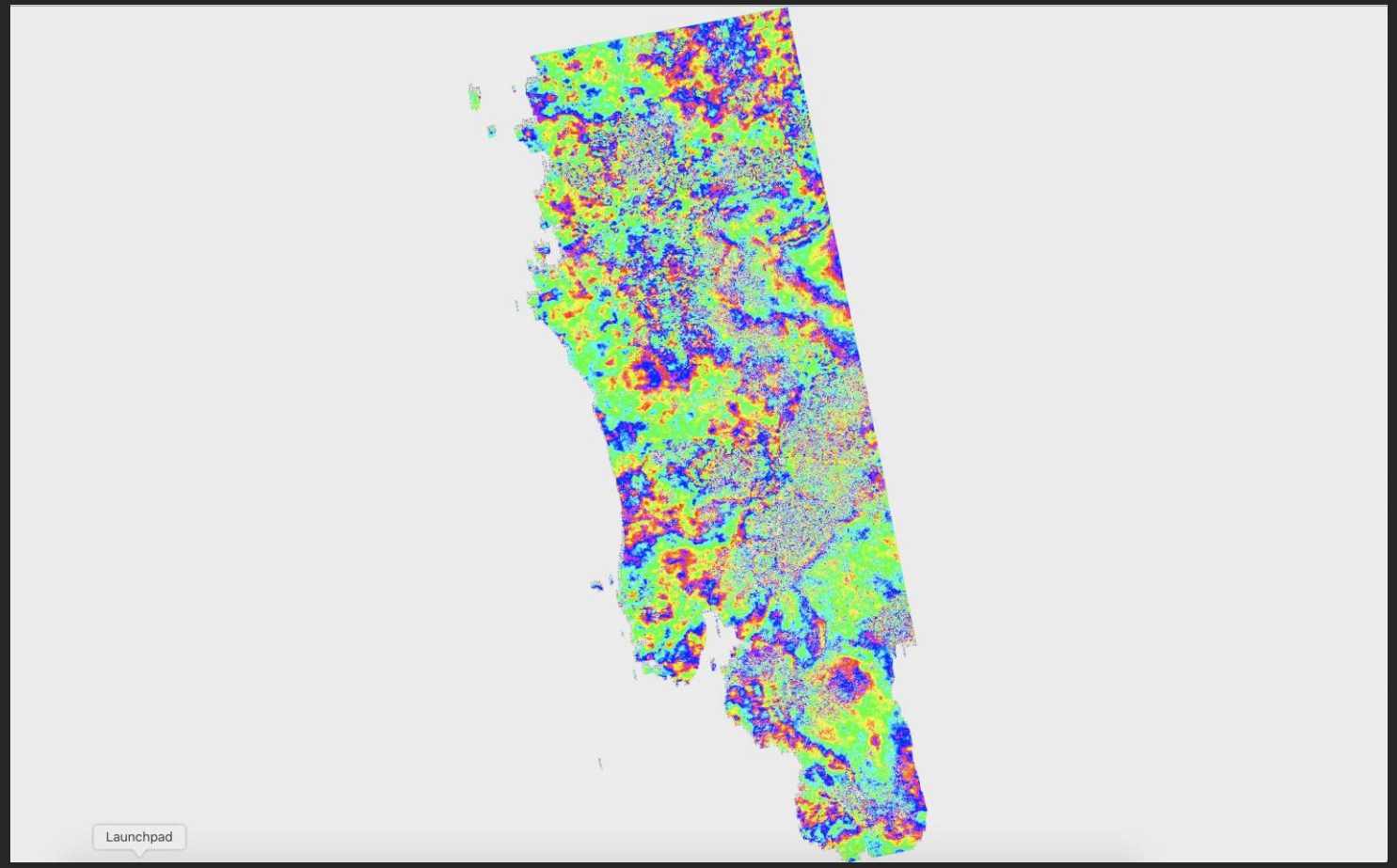

DInSAR processing softwares

- ISCE
  - Developed by the NASA-JPL
  - Doesn’t have GUI
  - Uses Python scripts to process InSAR images
  - This software could process many types of InSAR satellite data such as Sentinel 1, ALOS-2, Radarsat, Envisat
  - Among all the software used, ISCE is the fastest and the most flexible of them all

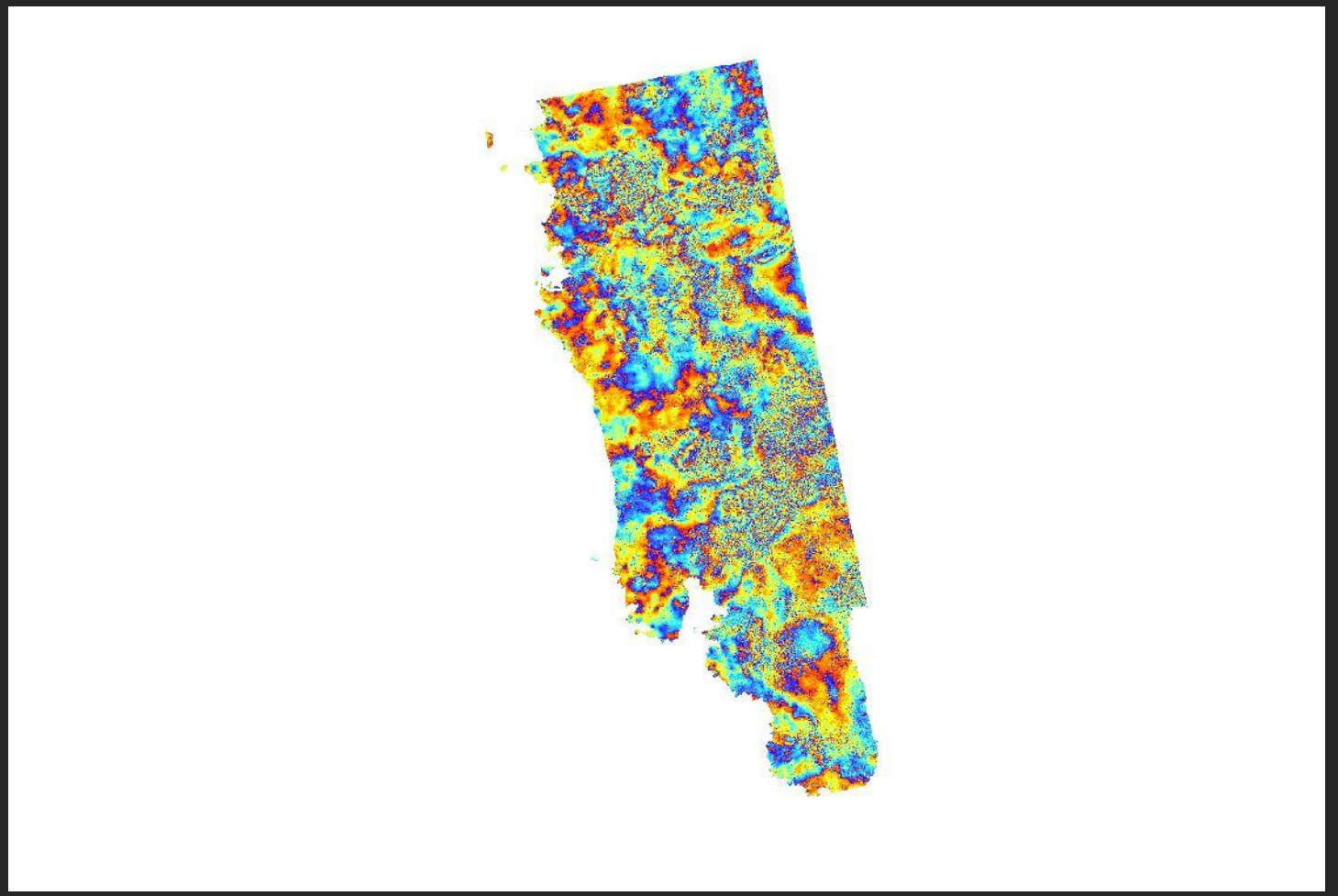

III. USES OF DINSAR

Uses of DInSAR for geohazard studies

- Earthquake
  - Identification of possible seismogenic fault
  - Measure coseismic slip and interseismic slip rate
- Volcano
  - Measurement of inflation and inflation rate
  - Measurement of viscoelastic response due to magma flow

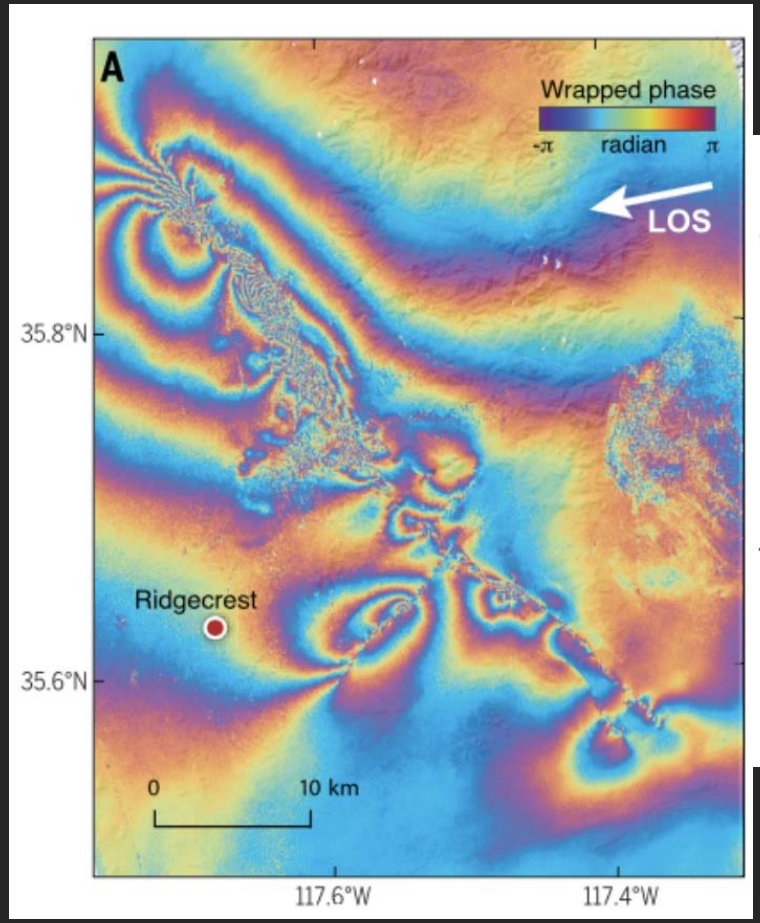

2019 M_W 6.4 and 7.1 Ridgecrest Earthquakes
Source: Ross et al., 2019

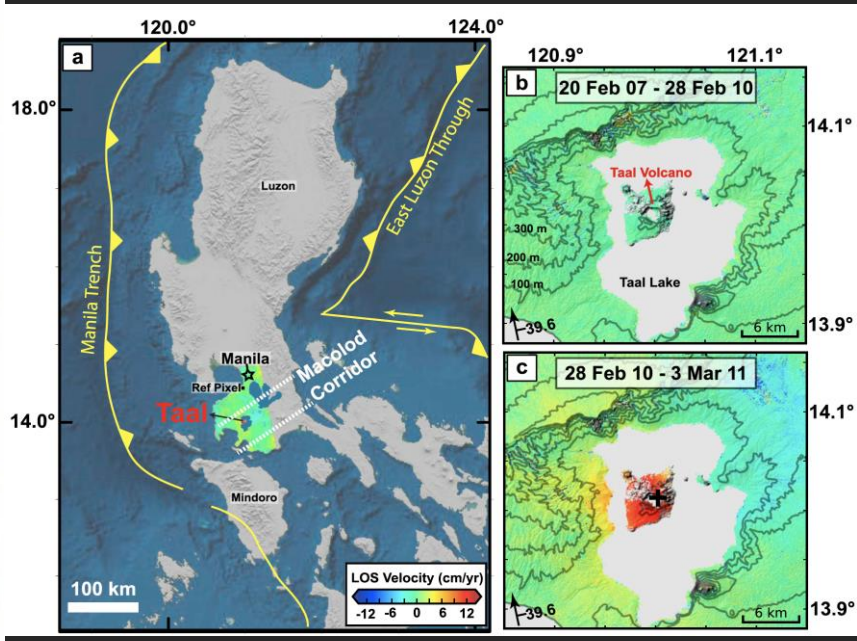

2010-2011 Taal volcano inflation event
Source: Morales Rivera et al., 2019

IV. OUTPUTS

EARTHQUAKES

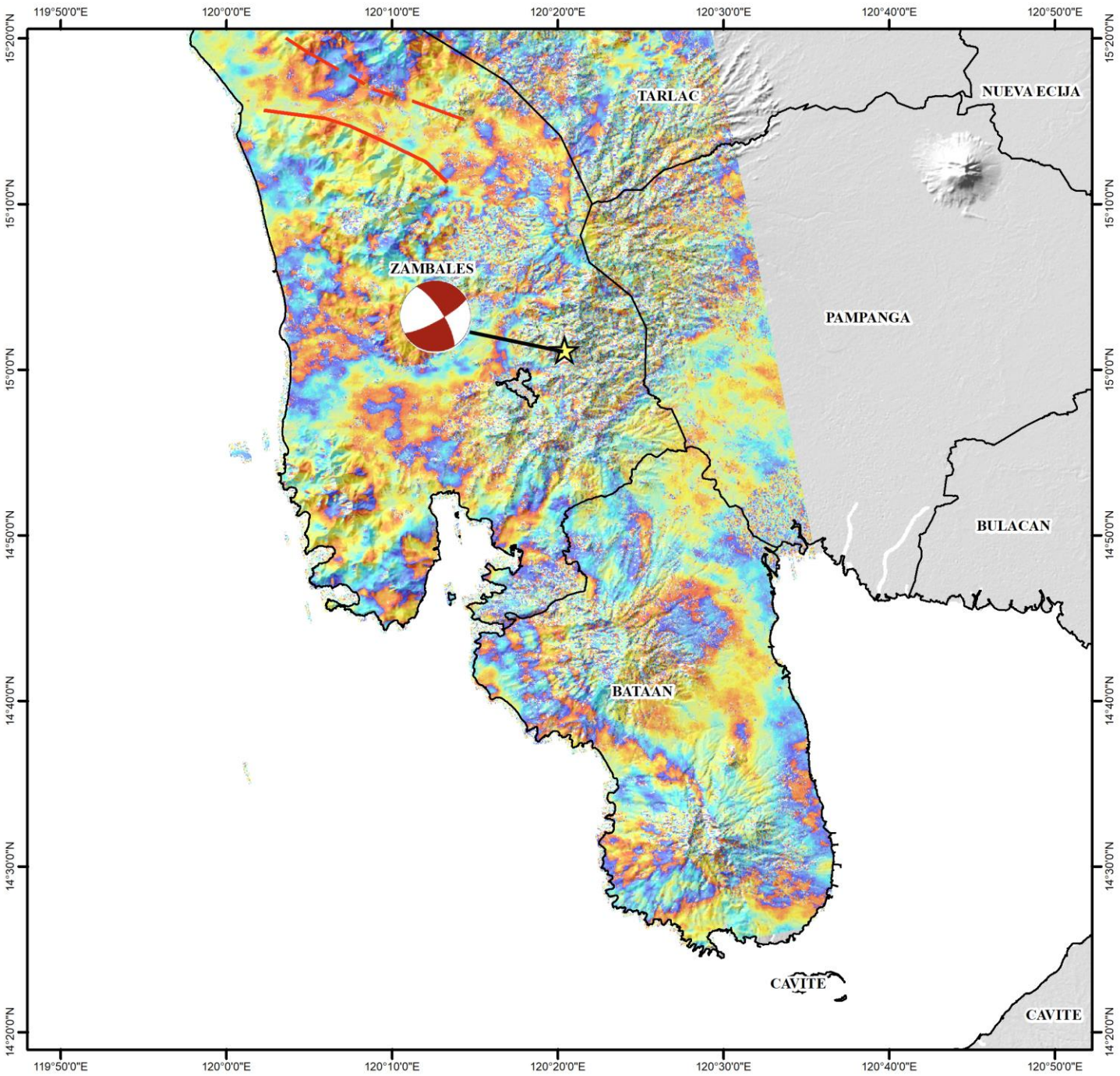

Phase Map of the 22 April 2019 M6.1 Central Luzon Earthquake

N

0 15 30

Kilometers

High : 3.14

Low : -3.14

Epicenter

Coordinate System: GCS WGS 1984
Datum: WGS 1984
Units: Degree

FD Azimuth

LOS Range

Acquisition Dates: 10 April 2019 (Pre-event)
22 April 2019 (Post-event)

Processing software: GMTSAR

Filters: Topography;
Power spectrum phase filtering;
Low coherence masking

Data Source: Sentinel 1B, ESA;
SRTM-DEM, NASA-JPL; Prov. Boundaries, PSA;
Active Faults and Focal Mechanism, PHIVOLCS

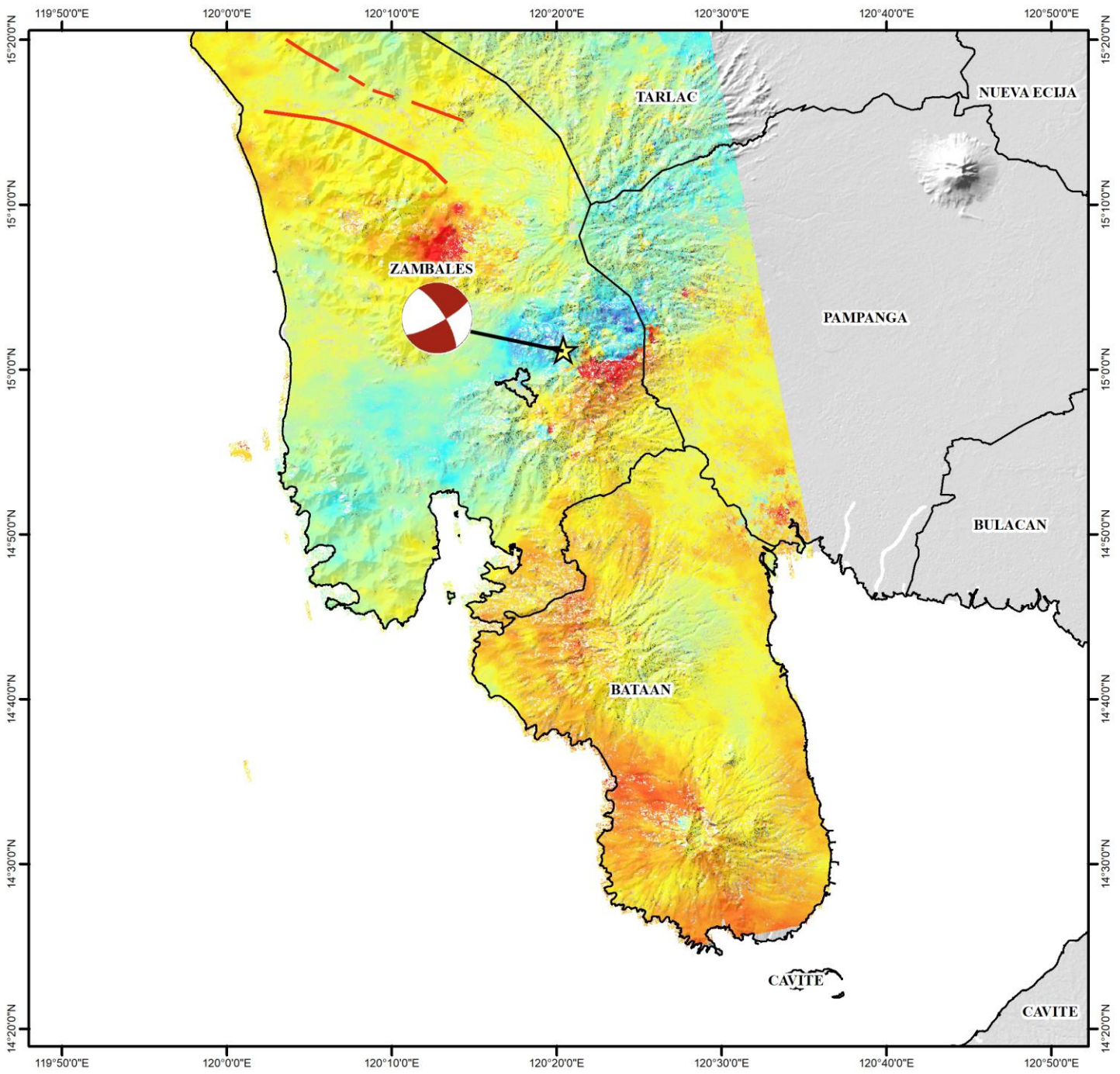

Line Of Sight Map of the 22 April 2019 M6.1 Central Luzon Earthquake

N

0 15 30

Kilometers

High : 106.091 mm

Low : -134.907 mm

Epicenter

Coordinate System: GCS WGS 1984
Datum: WGS 1984
Units: Degree

FD Azimuth

LOS Range

Acquisition Dates: 10 April 2019 (Pre-event)
22 April 2019 (Post-event)

Processing software: GMTSAR

Filters: Topography;
Power spectrum phase filtering;
Low coherence masking

Data Source: Sentinel 1B, ESA;
SRTM, NASA-JPL; Prov. Boundaries, PSA;
Active Faults and Focal Mechanism, PHIVOLCS

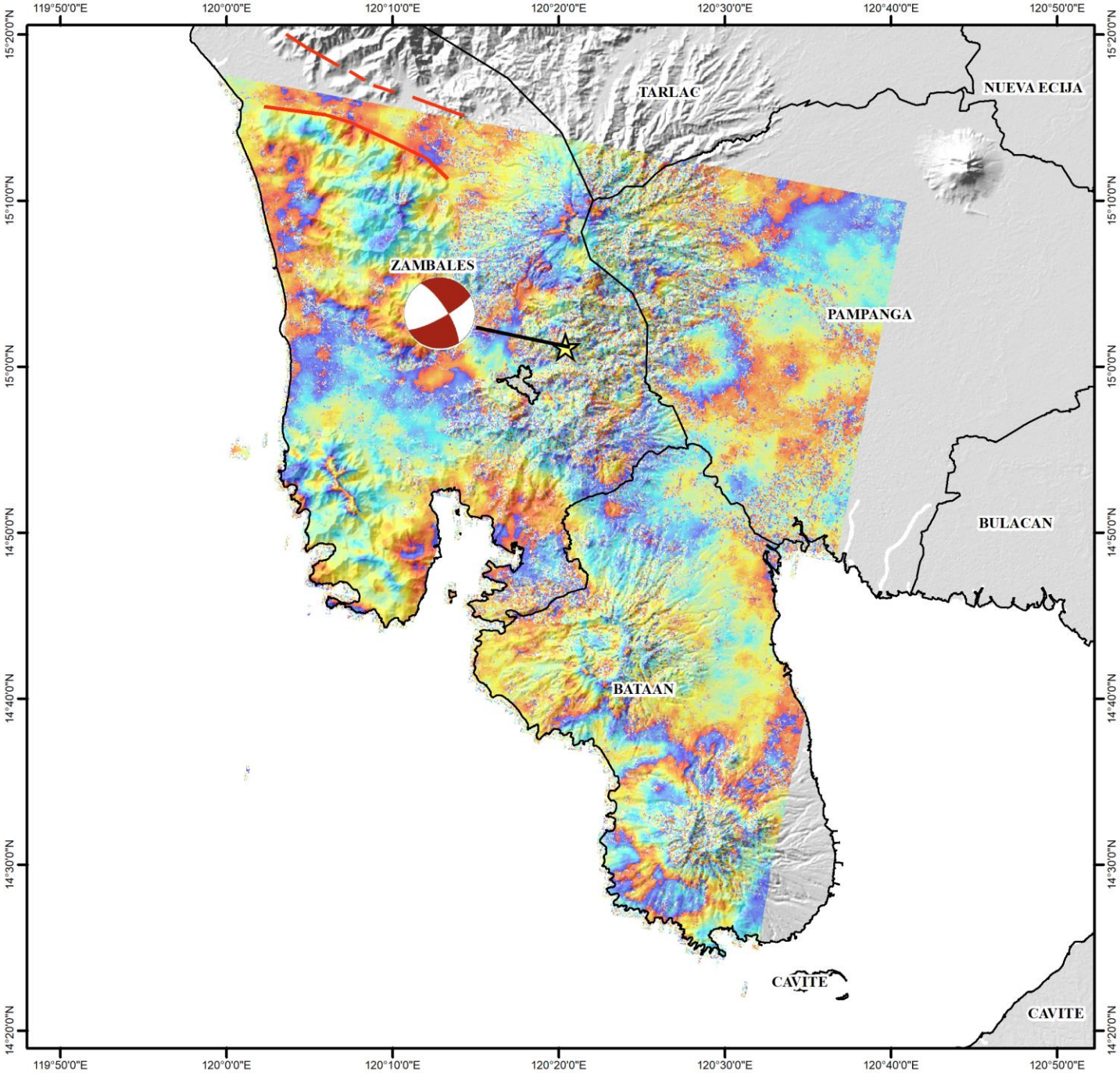

Phase Map of the 22 April 2019 M6.1 Central Luzon Earthquake

N

0 15 30

Kilometers

High : 3.14

Low : -3.14

Epicenter

Coordinate System: GCS WGS 1984
Datum: WGS 1984
Units: Degree

LOS Range

FD Azimuth

Acquisition Dates: 20 April 2019 (Pre-event)
02 May 2019 (Post-event)

Processing software: GMTSAR

Filters: Topography;
Power spectrum phase filtering;
Low coherence masking

Data Source: Sentinel 1A, ESA;
SRTM, NASA-JPL; Prov. Boundaries, PSA;
Active Faults and Focal Mechanism, PHIVOLCS

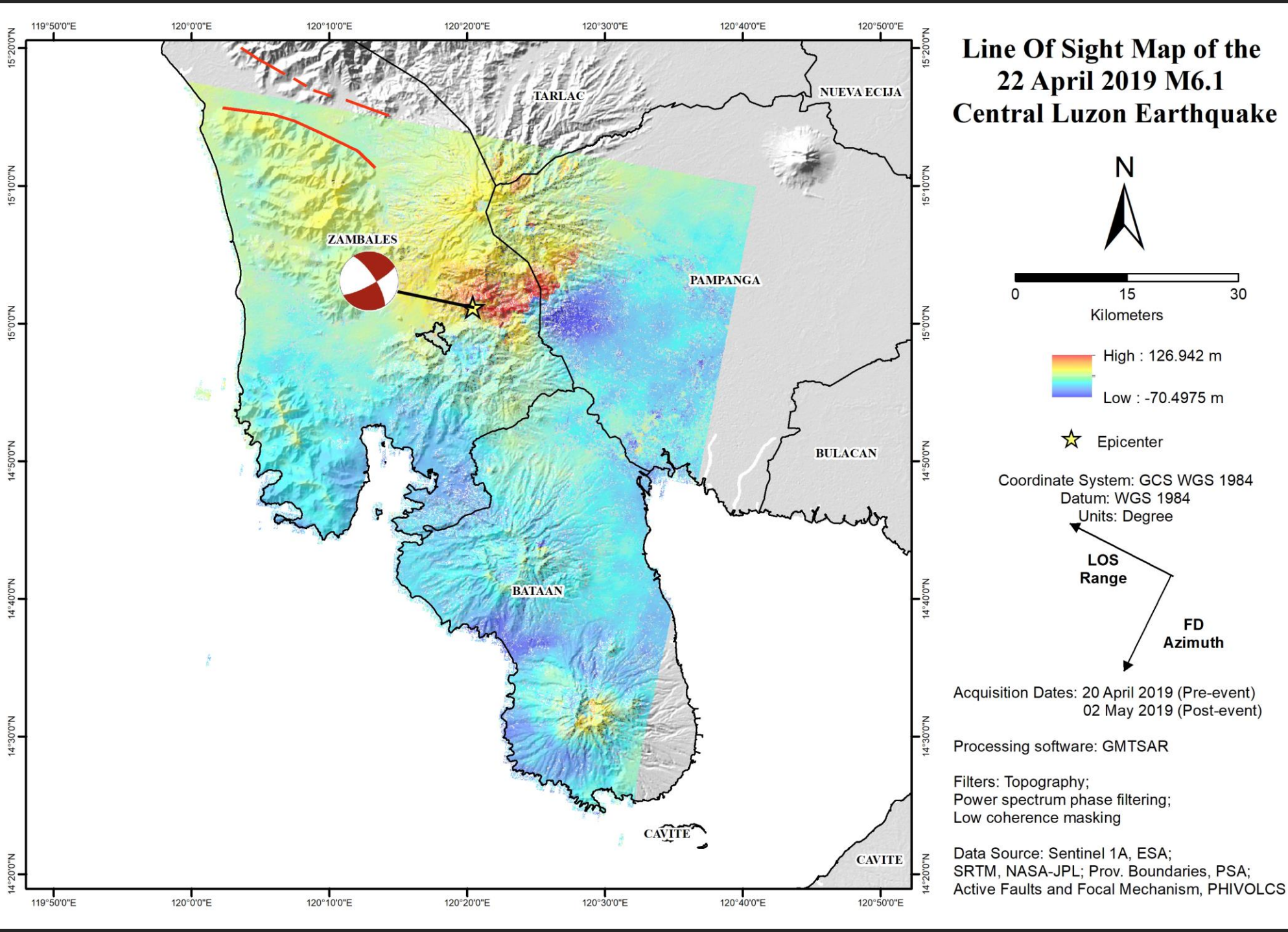

Line Of Sight Map of the 22 April 2019 M6.1 Central Luzon Earthquake

N

0 15 30

Kilometers

High : 126.942 m

Low : -70.4975 m

Epicenter

Coordinate System: GCS WGS 1984
Datum: WGS 1984
Units: Degree

LOS Range

FD Azimuth

Acquisition Dates: 20 April 2019 (Pre-event)
02 May 2019 (Post-event)

Processing software: GMTSAR

Filters: Topography;
Power spectrum phase filtering;
Low coherence masking

Data Source: Sentinel 1A, ESA;
SRTM, NASA-JPL; Prov. Boundaries, PSA;
Active Faults and Focal Mechanism, PHIVOLCS

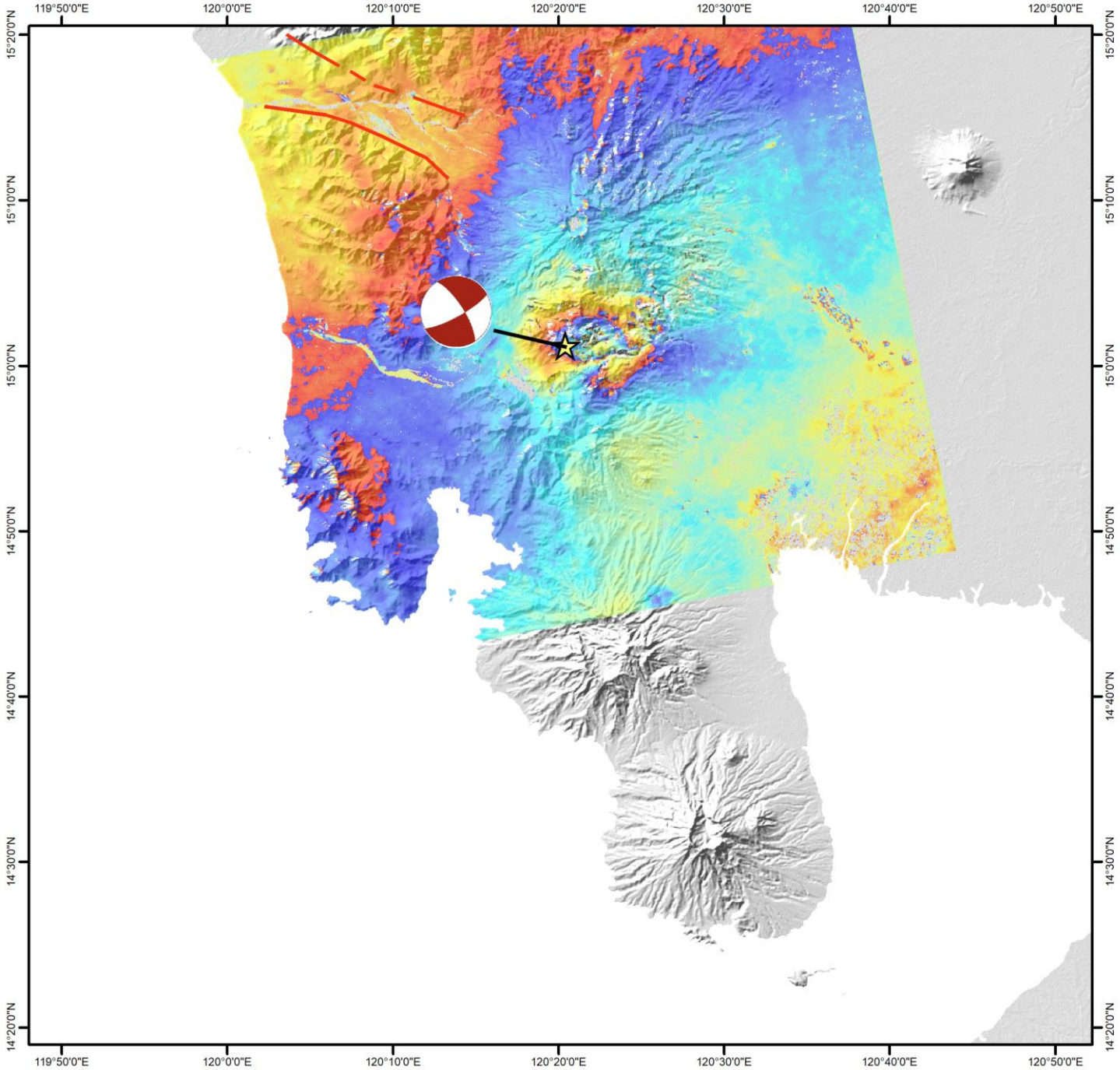

Phase Map of the 22 April 2019 M6.1 Central Luzon Earthquake

N

0 15 30

Kilometers

High : 3.14

Low : -3.14

Epicenter

Coordinate System: GCS WGS 1984
Datum: WGS 1984
Units: Degree

FD Azimuth

LOS Range

Acquisition Dates: 02 April 2019 (Pre-event)
30 April 2019 (Post-event)

Processing software: GMTSAR

Filters: Topography;
Power spectrum phase filtering;
Low coherence masking

Data Source: ALOS-2, JAXA;
SRTM, NASA-JPL; Prov. Boundaries, PSA;
Active Faults and Focal Mechanism, PHIVOLCS

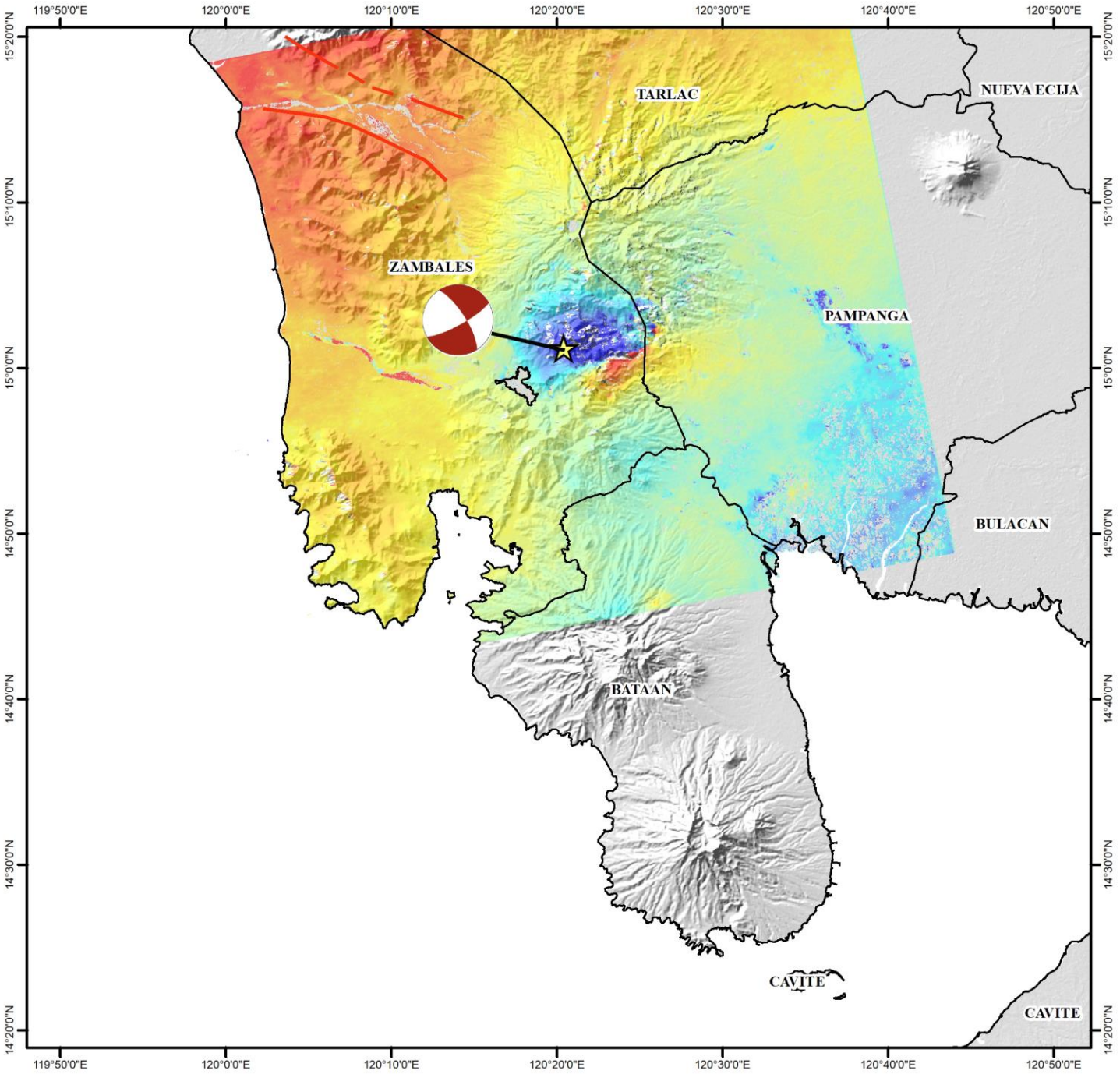

Line Of Sight Map of the 22 April 2019 M6.1 Central Luzon Earthquake

N

0 15 30

Kilometers

High : -29.0181 mm

Low : -442.499 mm

Epicenter

Coordinate System: GCS WGS 1984
Datum: WGS 1984
Units: Degree

FD Azimuth

LOS Range

Acquisition Dates: 02 April 2019 (Pre-event)
30 April 2019 (Post-event)

Processing software: GMTSAR

Filters: Topography;
Power spectrum phase filtering;
Low coherence masking

Data Source: ALOS-2, JAXA;
SRTM, NASA-JPL; Prov. Boundaries, PSA;
Active Faults and Focal Mechanism, PHIVOLCS

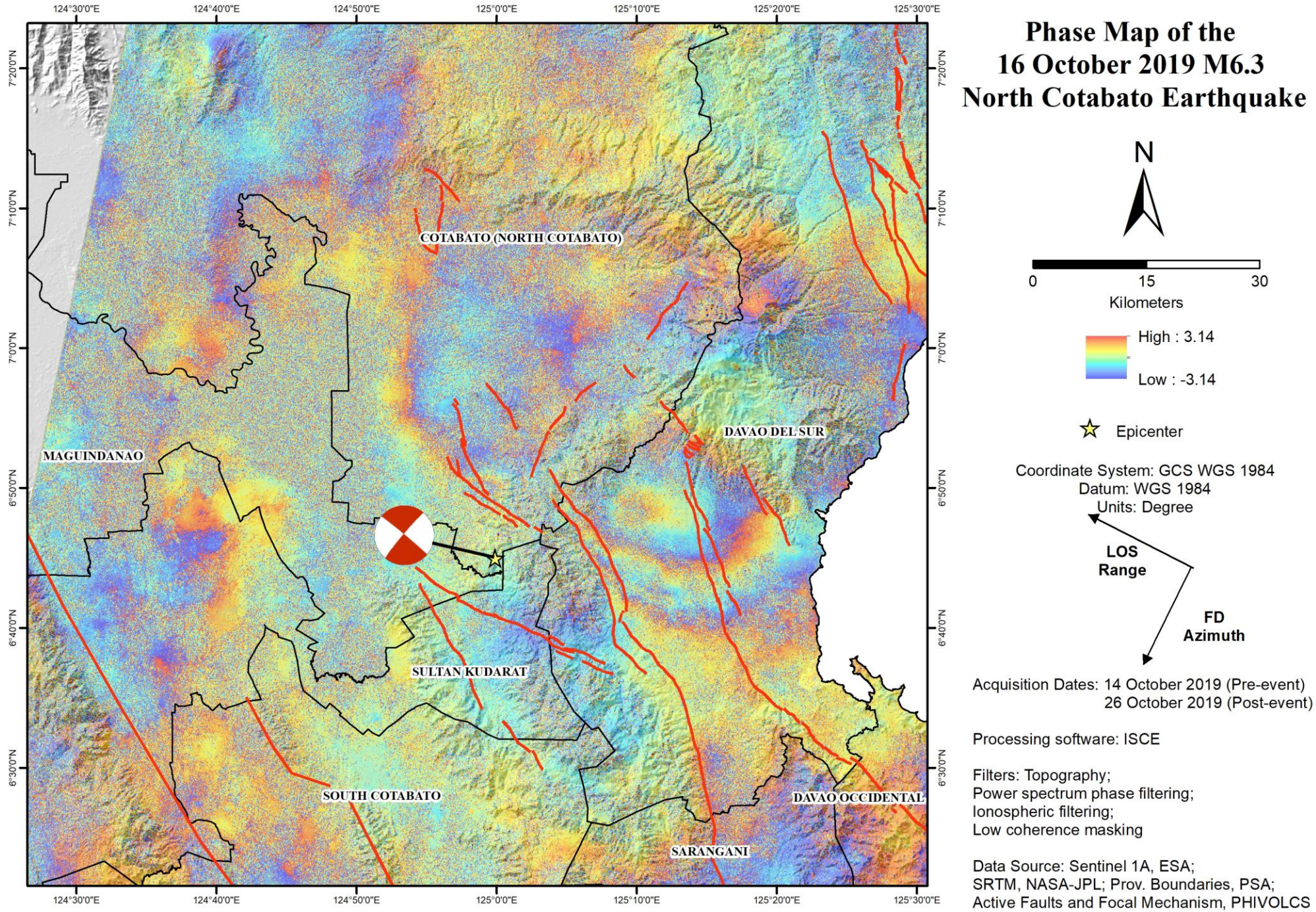

Phase Map of the 16 October 2019 M6.3 North Cotabato Earthquake

N

0 15 30

Kilometers

High : 3.14

Low : -3.14

Epicenter

Coordinate System: GCS WGS 1984
Datum: WGS 1984
Units: Degree

LOS Range

FD Azimuth

Acquisition Dates: 14 October 2019 (Pre-event)
26 October 2019 (Post-event)

Processing software: ISCE

Filters: Topography;
Power spectrum phase filtering;
Ionospheric filtering;
Low coherence masking

Data Source: Sentinel 1A, ESA;
SRTM, NASA-JPL; Prov. Boundaries, PSA;
Active Faults and Focal Mechanism, PHIVOLCS

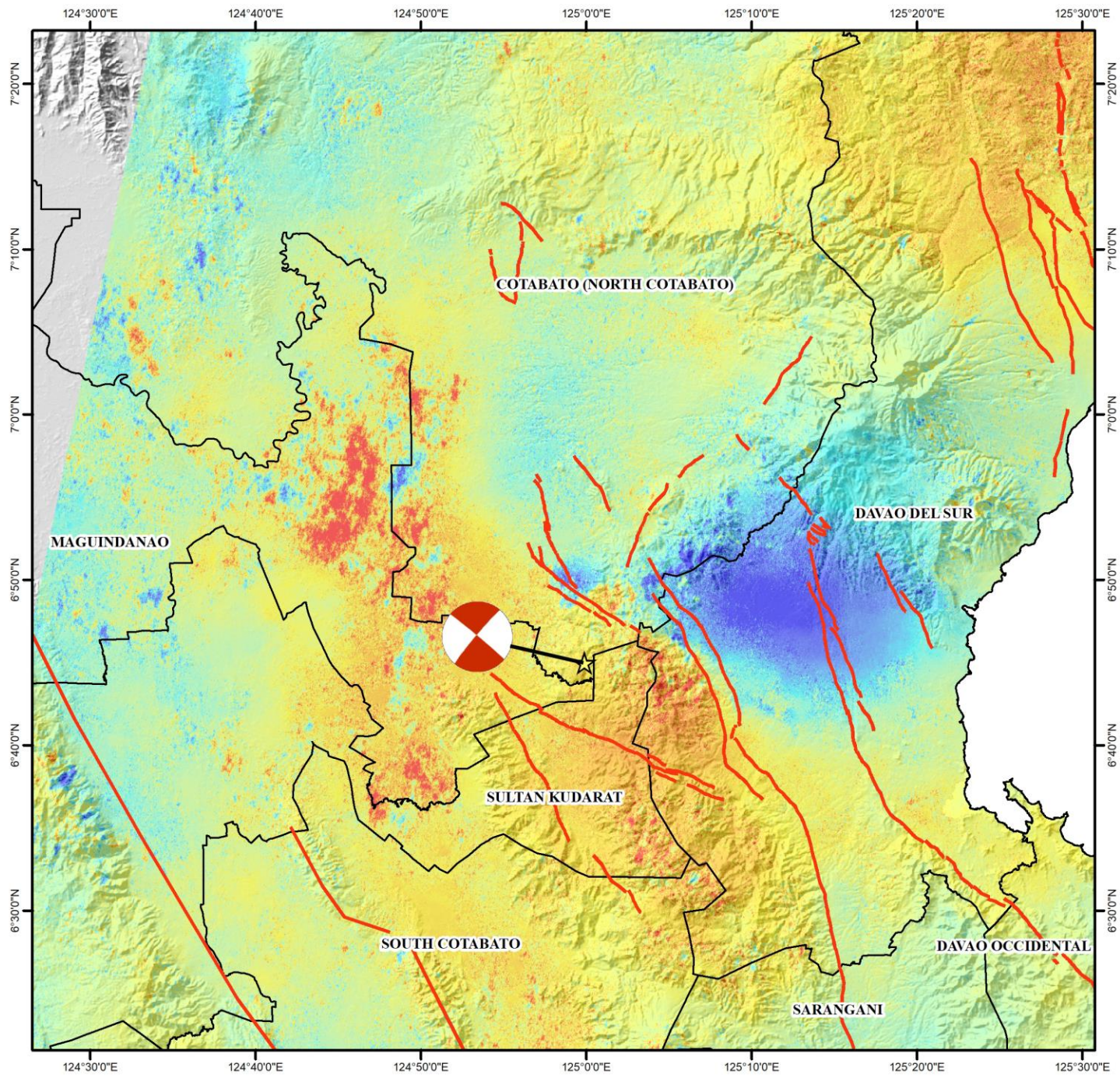

Line Of Sight Map of the 16 October 2019 M6.3 North Cotabato Earthquake

N

0 15 30

Kilometers

High : 95.294 mm

Low : -92.2991 mm

Epicenter

Coordinate System: GCS WGS 1984
Datum: WGS 1984
Units: Degree

LOS Range

FD Azimuth

Acquisition Dates: 14 October 2019 (Pre-event)
26 October 2019 (Post-event)

Processing software: ISCE

Filters: Topography;
Power spectrum phase filtering;
Ionospheric filtering;
Low coherence masking

Data Source: Sentinel 1A, ESA;
SRTM, NASA-JPL; Prov. Boundaries, PSA;
Active Faults and Focal Mechanism, PHIVOLCS

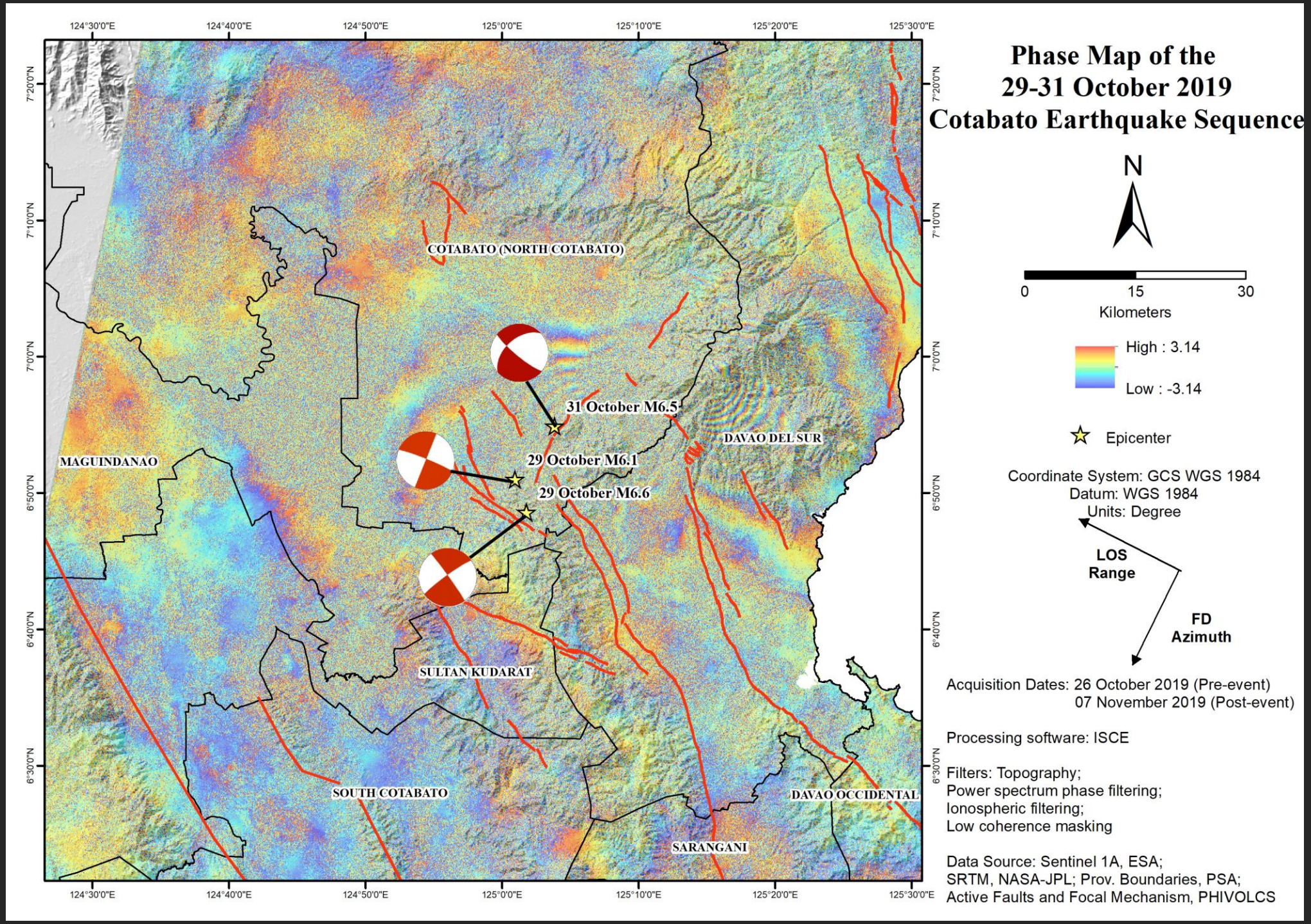
124°30'0"E
124°40'0"E
124°50'0"E
125°0'0"E
125°10'0"E
125°20'0"E
125°30'0"E
7°20'0"N
7°10'0"N
7°0'0"N
6°50'0"N
6°40'0"N
6°30'0"N
COTABATO (NORTH COTABATO)
MAGUINDANAO
DAVAO DEL SUR
SULTAN KUDARAT
SOUTH COTABATO
DAVAO OCCIDENTAL
SARANGANI
31 October M6.5
29 October M6.1
29 October M6.6
Phase Map of the
29-31 October 2019
Cotabato Earthquake Sequence
N
0
15
30
Kilometers
High : 3.14
Low : -3.14
Epicenter
Coordinate System: GCS WGS 1984
Datum: WGS 1984
Units: Degree
LOS
Range
FD
Azimuth
Acquisition Dates: 26 October 2019 (Pre-event)
07 November 2019 (Post-event)
Processing software: ISCE
Filters: Topography;
Power spectrum phase filtering;
Ionospheric filtering;
Low coherence masking
Data Source: Sentinel 1A, ESA;
SRTM, NASA-JPL; Prov. Boundaries, PSA;
Active Faults and Focal Mechanism, PHIVOLCS

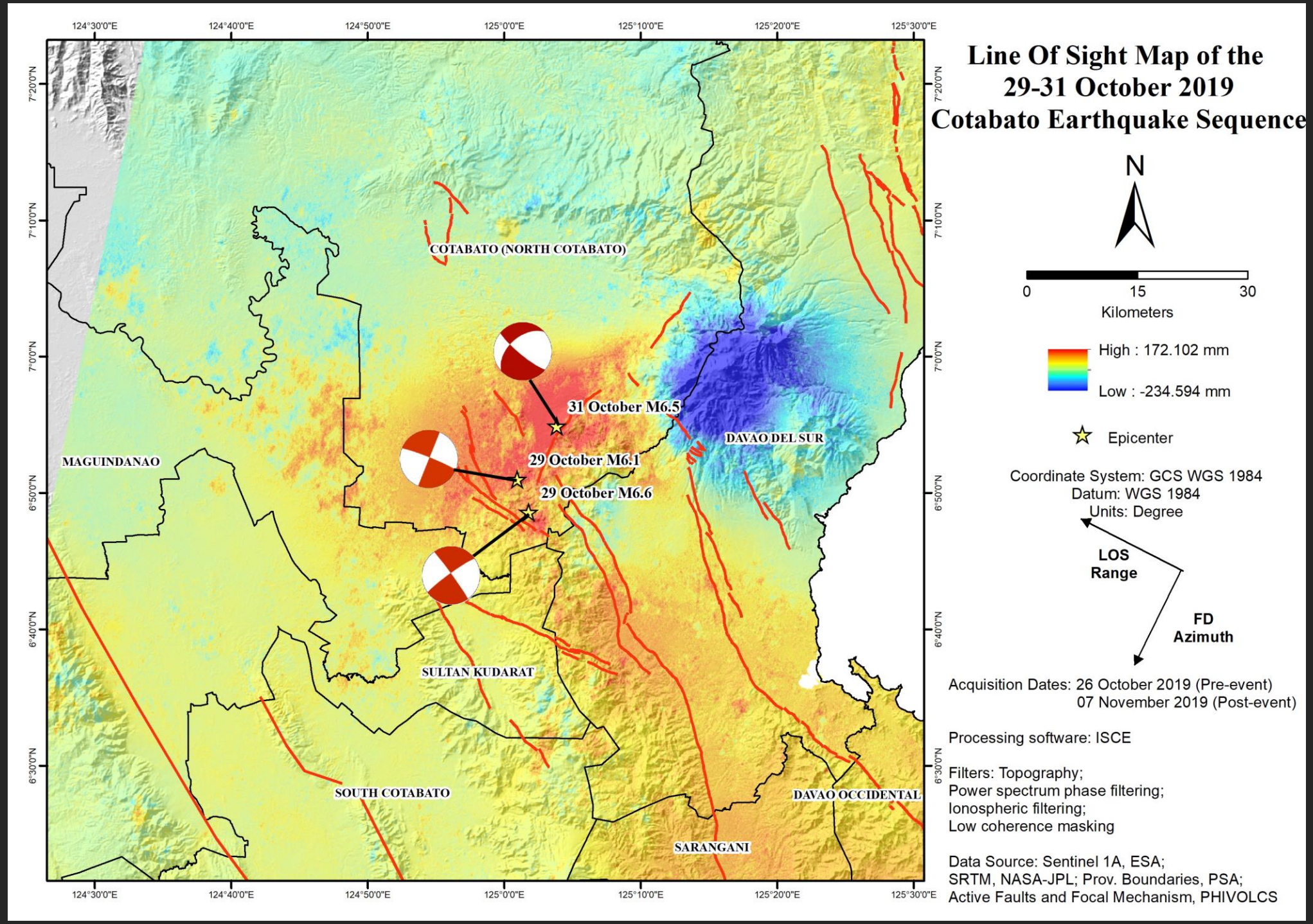
Line Of Sight Map of the
29-31 October 2019
Cotabato Earthquake Sequence
N
0
15
30
Kilometers
High : 172.102 mm
Low : -234.594 mm
Epicenter
Coordinate System: GCS WGS 1984
Datum: WGS 1984
Units: Degree
LOS
Range
FD
Azimuth
Acquisition Dates: 26 October 2019 (Pre-event)
07 November 2019 (Post-event)
Processing software: ISCE
Filters: Topography;
Power spectrum phase filtering;
Ionospheric filtering;
Low coherence masking
Data Source: Sentinel 1A, ESA;
SRTM, NASA-JPL; Prov. Boundaries, PSA;
Active Faults and Focal Mechanism, PHIVOLCS
COTABATO (NORTH COTABATO)
MAGUINDANAO
DAVAO DEL SUR
SULTAN KUDARAT
SOUTH COTABATO
DAVAO OCCIDENTAL
SARANGANI
31 October M6.5
29 October M6.1
29 October M6.6
124°30'0"E
124°40'0"E
124°50'0"E
125°0'0"E
125°10'0"E
125°20'0"E
125°30'0"E
7°20'0"N
7°10'0"N
7°0'0"N
6°50'0"N
6°40'0"N
6°30'0"N

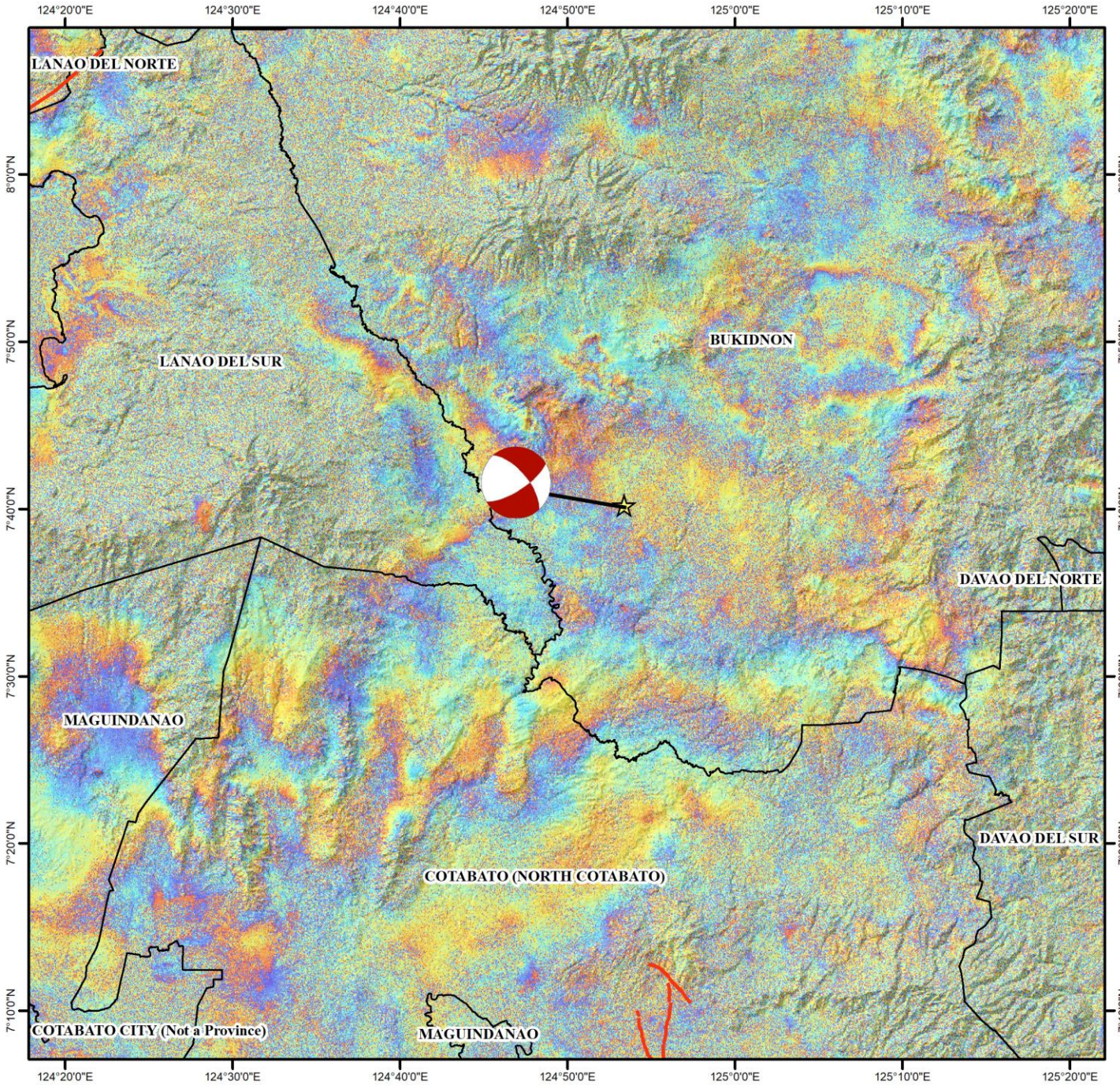

Phase Map of the 18 November 2019 M5.9 Southern Bukidnon Earthquake

N

0 15 30

Kilometers

High : 3.14

Low : -3.14

Epicenter

Coordinate System: GCS WGS 1984
Datum: WGS 1984
Units: Degree

FD Azimuth

LOS Range

Acquisition Dates: 07 November 2019 (Pre-event)
19 November 2019 (Post-event)

Processing software: ISCE

Filters: Topography;
Power spectrum phase filtering;
Ionospheric filtering;
Low coherence masking

Data Source: Sentinel 1B, ESA;
SRTM-DEM, NASA-JPL; Prov. Boundaries, PSA;
Active Faults and Focal Mechanism, PHIVOLCS

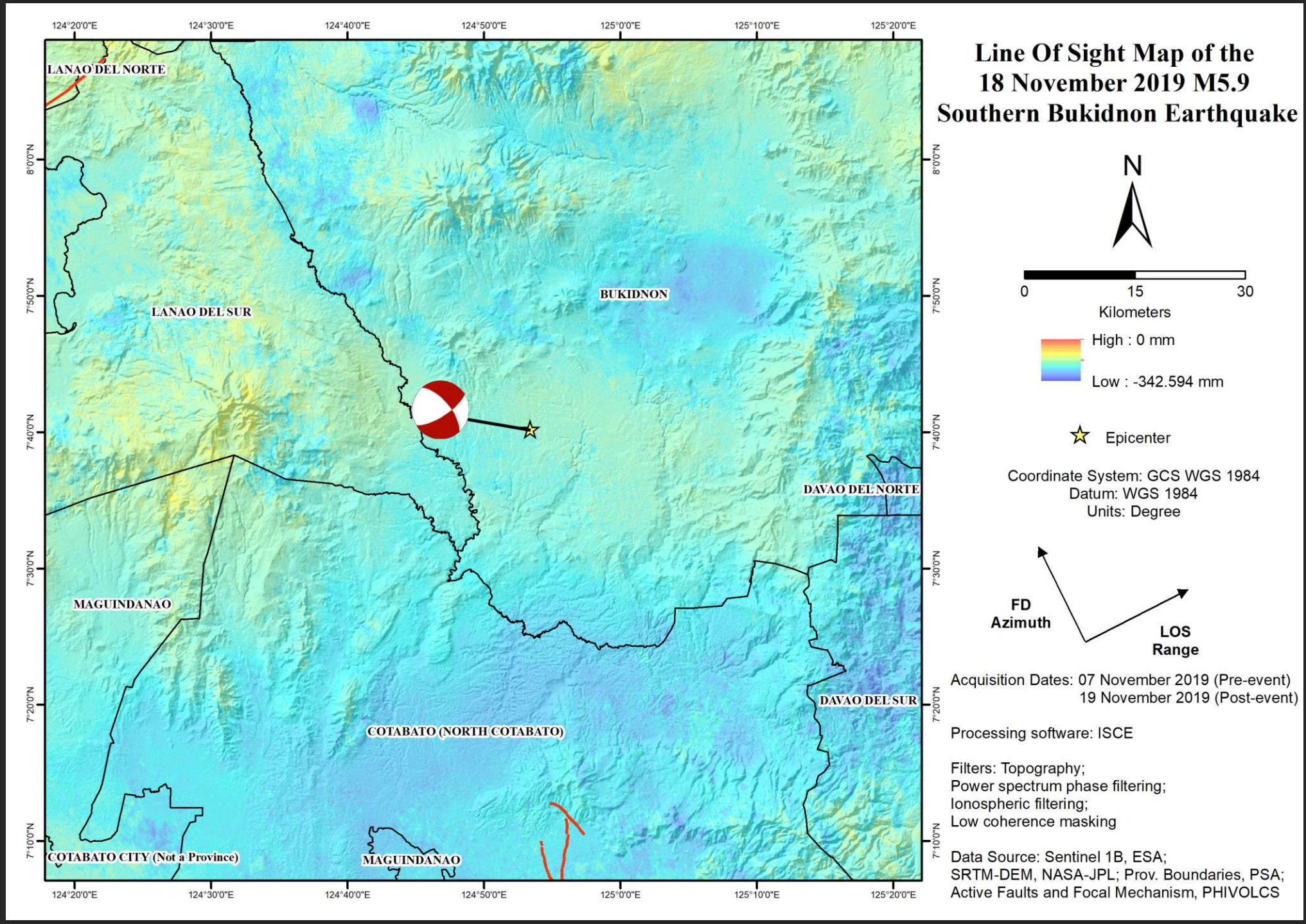

Line Of Sight Map of the 18 November 2019 M5.9 Southern Bukidnon Earthquake

N

0 15 30

Kilometers

High : 0 mm

Low : -342.594 mm

Epicenter

Coordinate System: GCS WGS 1984
Datum: WGS 1984
Units: Degree

FD Azimuth

LOS Range

Acquisition Dates: 07 November 2019 (Pre-event)
19 November 2019 (Post-event)

Processing software: ISCE

Filters: Topography;
Power spectrum phase filtering;
Ionospheric filtering;
Low coherence masking

Data Source: Sentinel 1B, ESA;
SRTM-DEM, NASA-JPL; Prov. Boundaries, PSA;
Active Faults and Focal Mechanism, PHIVOLCS

VOLCANO

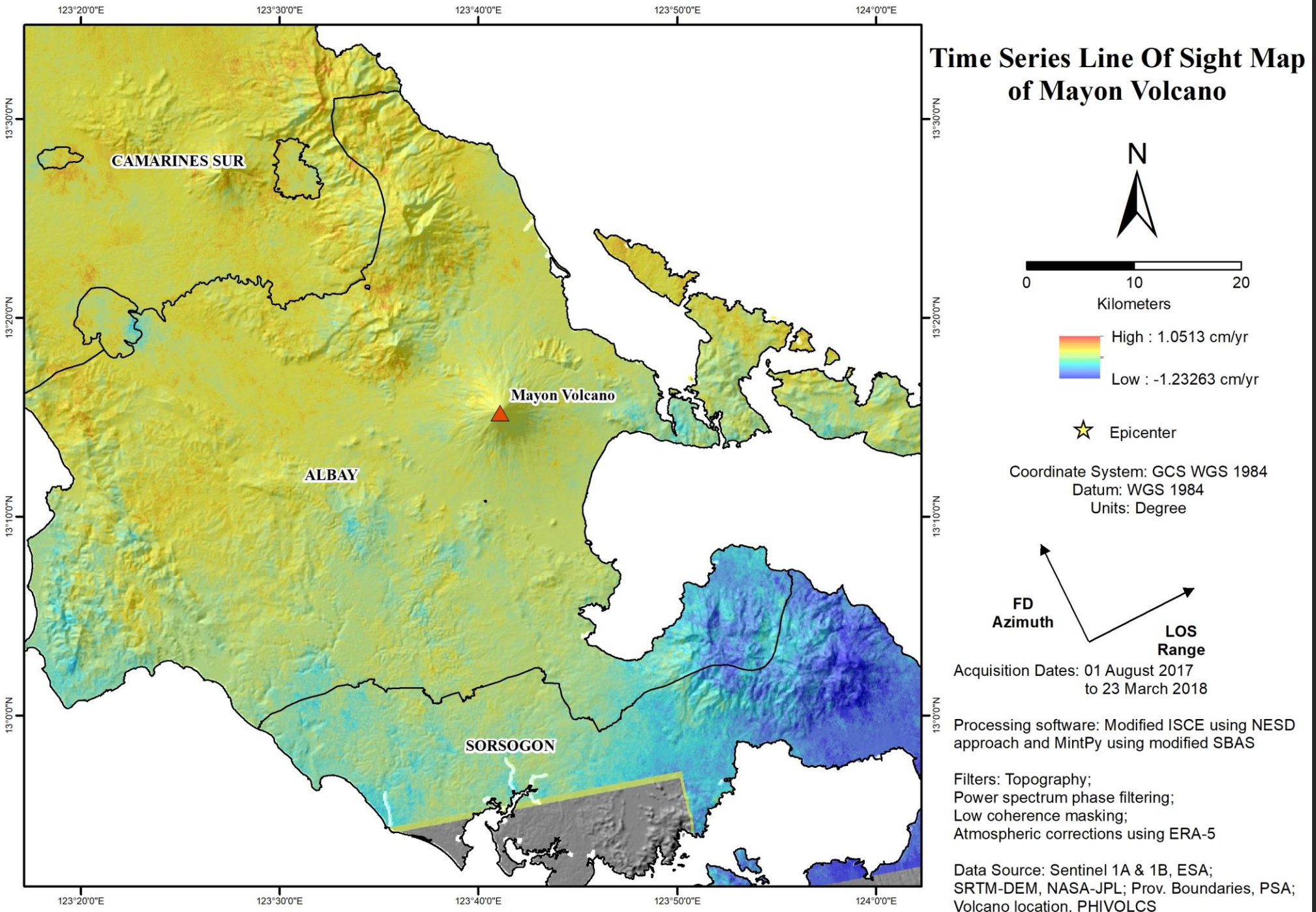

Time Series Line Of Sight Map of Mayon Volcano

N

0 10 20

Kilometers

High : 1.0513 cm/yr

Low : -1.23263 cm/yr

Epicenter

Coordinate System: GCS WGS 1984
Datum: WGS 1984
Units: Degree

FD Azimuth

LOS Range

Acquisition Dates: 01 August 2017 to 23 March 2018

Processing software: Modified ISCE using NESD approach and MintPy using modified SBAS

Filters: Topography;
Power spectrum phase filtering;
Low coherence masking;
Atmospheric corrections using ERA-5

Data Source: Sentinel 1A & 1B, ESA;
SRTM-DEM, NASA-JPL; Prov. Boundaries, PSA;
Volcano location, PHIVOLCS

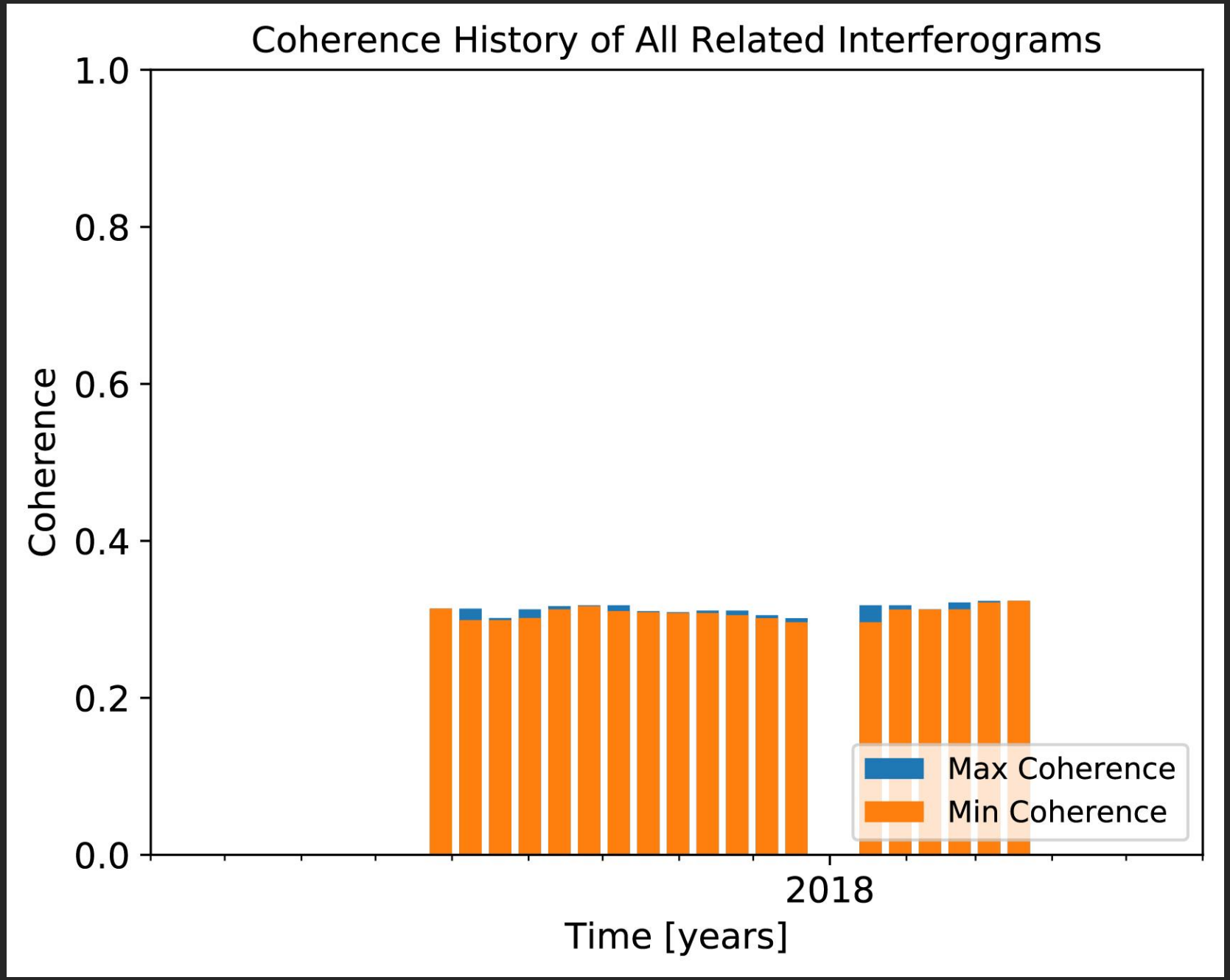
Coherence History of All Related Interferograms
1.0
0.8
0.6
0.4
0.2
0.0
Coherence
2018
Time [years]
Max Coherence
Min Coherence

V. Conclusion

- DInSAR is an effective tool in detecting earthquake ground deformation
  - However, sensor limitations, atmospheric conditions and ground manifestation of the earthquake may result to non-detection
- Non-detection of volcano inflation/deflation trend using time-series methods from DInSAR due to low coherence of the interferogram networks
  - Could be improved if L-band satellites (e.g. ALOS-2) are used instead of C-band satellites (e.g. Sentinel 1) which are more sensitive to ground deformation

VII. Way Forward

- Forward modeling using known earthquake parameters to properly constrain the interferogram related to the earthquake
- Acquire ALOS-2 satellite data to detect volcano inflation/deflation trend

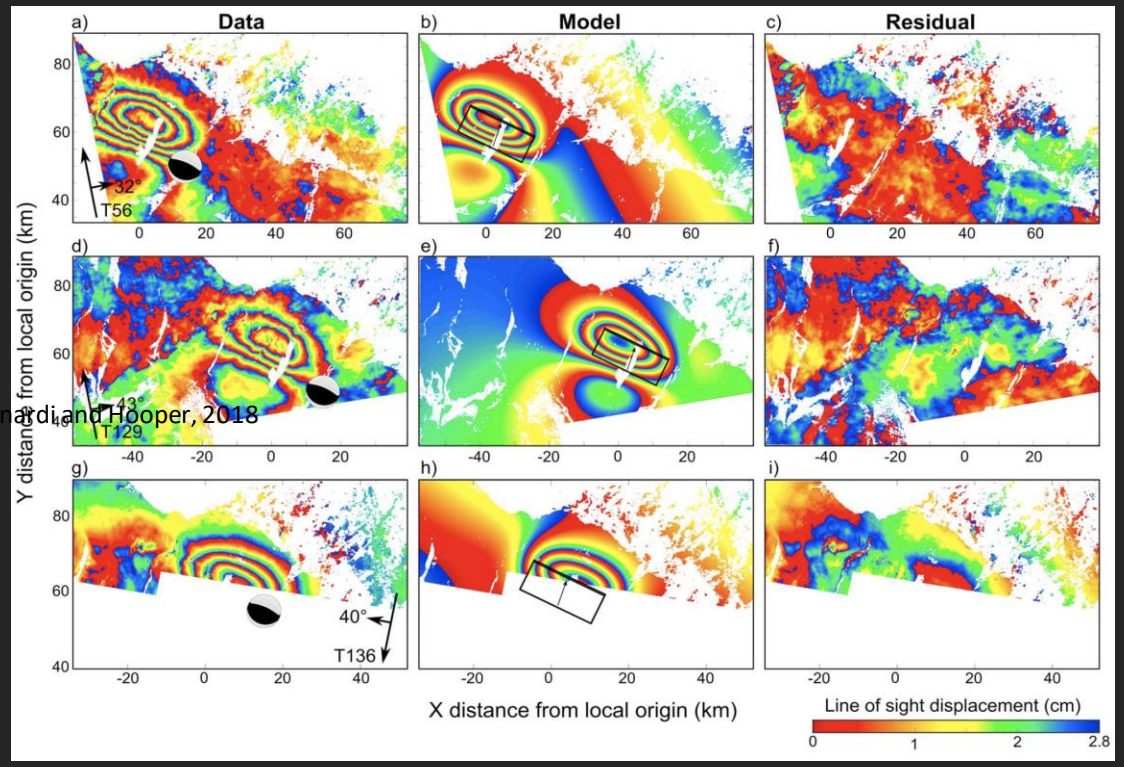

Bagnardi and Hooper, 2018

References

- Bagnardi, M., Hooper, A., 2018. Inversion of Surface Deformation Data for Rapid Estimates of Source Parameters and Uncertainties: A Bayesian Approach. Geochemistry, Geophys. Geosystems 19, 2194–2211. https://doi.org/10.1029/2018GC007585
- Berardino, P., Fornaro, G., Lanari, R., Sansosti, E., 2002. A new algorithm for surface deformation monitoring based on small baseline differential SAR interferograms. IEEE Trans. Geosci. Remote Sens. 40, 2375–2383. https://doi.org/10.1109/TGRS.2002.803792
- De Zan, F., Guarnieri, A.M., 2006. TOPSAR: Terrain observation by progressive scans. IEEE Trans. Geosci. Remote Sens. 44, 2352–2360. https://doi.org/10.1109/TGRS.2006.873853
- ESA, 2019a. Satellite Description [WWW Document]. Sentin. Online.
- ESA, 2019b. Instrument Payload [WWW Document]. Sentin. Online. URL https://sentinel.esa.int/web/sentinel/missions/sentinel-1/instrument-payload (accessed 9.20.19).
- Fattahi, H., Agram, P., Simons, M., 2017. A Network-Based Enhanced Spectral Diversity Approach for TOPS Time-Series Analysis. IEEE Trans. Geosci. Remote Sens. 55, 777–786. https://doi.org/10.1109/TGRS.2016.2614925
- Fletcher, K., Agency., E.S., Centre., E.S.R. and T., 2007. InSAR principles : guidelines for SAR interferometry processing and interpretation. ESA Publications Division, ESTEC, Noordwijk, the Netherlands.
- Hennig, S., 2013. Exploring the Benefits of Active vs. Passive Spaceborne Systems [WWW Document]. Earth Imaging J.
- JAXA, 2014. ALOS-2 Project / ALOS-2 Overview [WWW Document].
- Liang, C., Fielding, E.J., 2017. Interferometry with ALOS-2 Full-Aperture ScanSAR Data. IEEE Trans. Geosci. Remote Sens. 55, 2739–2750. https://doi.org/10.1109/TGRS.2017.2653190
- Lillesand, T.M., Kiefer, R.W., Chipman, J.W., 2015. Remote sensing and image interpretation, 7th ed. Wiley, Danvers.

References

- Lindsey, E.O., Natsuaki, R., Xu, X., Shimada, M., Hashimoto, M., Melgar, D., Sandwell, D.T., 2015. Line-of-sight displacement from ALOS-2 interferometry: Mw 7.8 Gorkha Earthquake and Mw 7.3 aftershock. Geophys. Res. Lett. 42, 6655–6661. https://doi.org/10.1002/2015GL065385
- Morales Rivera, A.M., Amelung, F., Albino, F., Gregg, P.M., 2019. Impact of Crustal Rheology on Temperature-Dependent Viscoelastic Models of Volcano Deformation: Application to Taal Volcano, Philippines. J. Geophys. Res. Solid Earth 124, 978–994. https://doi.org/10.1029/2018JB016054
- Moreira, A., Prats-Iraola, P., Younis, M., Krieger, G., Hajnsek, I., Papathanassiou, K.P., 2013. A tutorial on synthetic aperture radar. IEEE Geosci. Remote Sens. Mag. 1, 6–43. https://doi.org/10.1109/MGRS.2013.2248301
- OpenStax, 2019. The Electromagnetic Spectrum [WWW Document]. LibreTexts.
- Pham, D.T., Yokoya, N., Bui, T.D., Yoshino, K., Friess, A.D., 2019. Remote Sensing Approaches for Monitoring Mangrove Species, Structure, and Biomass: Opportunities and Challenges. Remote Sens. . https://doi.org/10.3390/rs11030230
- Simons, M., Rosen, P.A., 2015. Interferometric Synthetic Aperture Radar Geodesy, in: Schubert, G. (Ed.), Treatise on Geophysics. Elsevier, pp. 339–385. https://doi.org/http://dx.doi.org/10.1016/B978-0-444-53802-4.00061-0
- Tian, X., Malhotra, R., Xu, B., Qi, H., Ma, Y., 2018. Modeling Orbital Error in InSAR Interferogram Using Frequency and Spatial Domain Based Methods. Remote Sens. . https://doi.org/10.3390/rs10040508
- Valkaniotis, S.., Foumelis, M., Ganas, A., 2017. A preliminary report on the Jul. 6, 2017 M=6.5 Philippines earthquake.
- Yunjun, Z., Fattahi, H., Amelung, F., 2019. Small baseline InSAR time series analysis: Unwrapping error correction and noise reduction. Comput. Geosci. 133, 104331. https://doi.org/10.1016/j.cageo.2019.10433

THANK YOU FOR LISTENING!